CHAPTER 3 MATERIALS AND METHODS

3.1 Numerical model of wheel rail contact

In this section, a finite element models using Abaqus CAE 2020 software, is implemented for numerical analysis of the contact between the rail and wheel. First, the geometrical model of both the wheel and the rail are developed according to the parameters from the ERC data. Then, this model was used for finite element analysis.

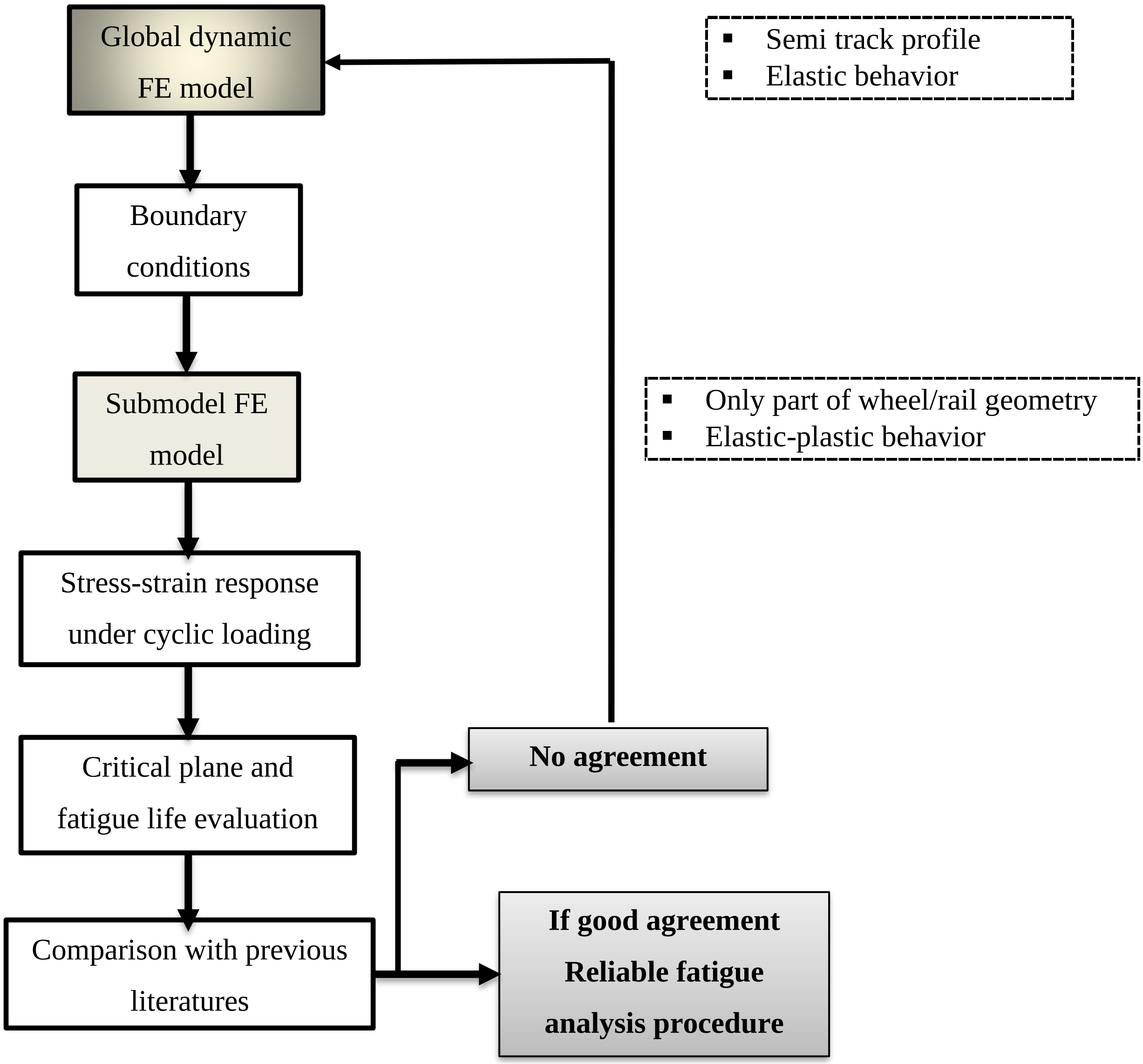

Figure 3-1 Flow chart of wheel fatigue analysis

3.1.1 Geometrical modelling

The two-dimensional curve the wheel profile is revolved within a radius of 330 mm to create the three-dimensional geometric model of the wheel. Whereas, the 3D rail model is generated by extruding railhead profile curve by a distance of 600 mm (the distance between slippers).

3.1.1.1 Wheel and rail geometries

The point of contact is established so that the wheel tread center and the rail head center are aligned, as shown in Figure 3-2.

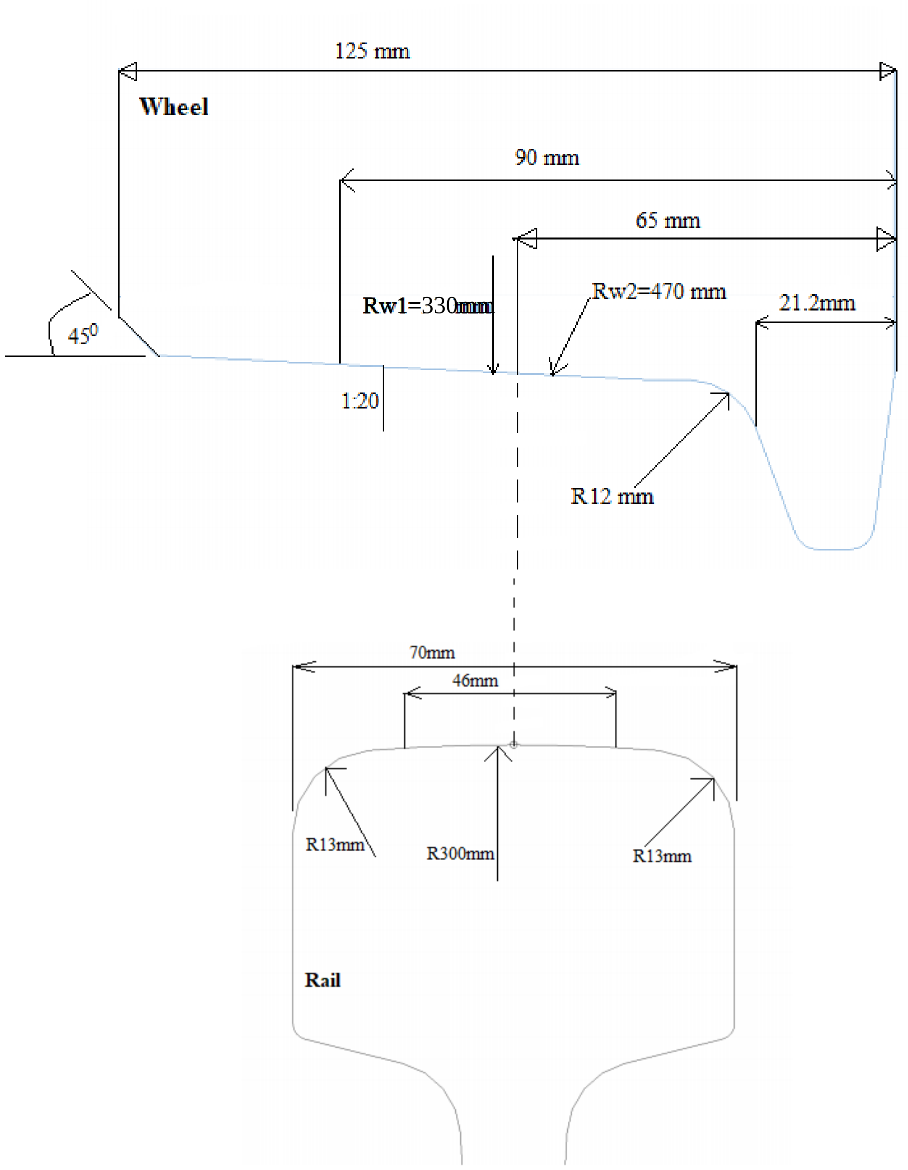

Figure 3-2 Wheel and Rail geometry model

Table 3-1 Geometry parameters of wheel and rail [27]

Wheel					Rail	
Radius(Rw1)	Contact curvature(Rw2)	Flange thickness(e)	Flange height(h)	Rim nominal width(L)	Radius (Rr1)	Contact curvature (Rr2)
330 mm	470mm	21.21mm	28mm	130mm	∞	300mm

First the rail and the wheel are created separately using the Abaqus CAD section. The 3D part files were generated by extruding (for the rail) and revolving (for the wheel) using the 2D drawing primarily created as in Figure 3-3. The rail was extruded for length of 600mm (the length between the sleepers). The assembly tool is used to bring the files together as shown in Figure 3-3 to create the whole model.

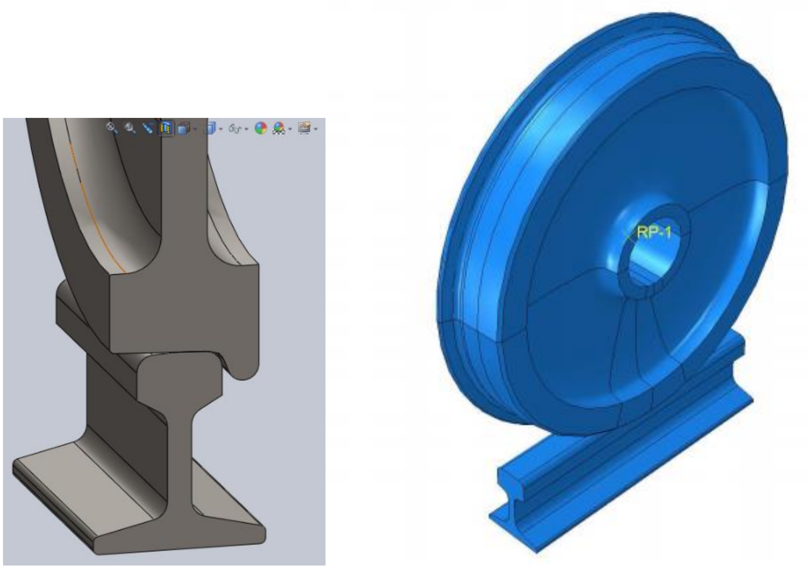

Figure 3-3 Assembly geometry of wheel and rail

3.1.1 Finite element model (FEM)

In this part, the geometry developed in the CAD environment of Abaqus is used for numerical analysis. In order to combine the global response with the local response two models were used. The first model is called the global model in which one of the wheels is permitted to roll over 600 mm (the length between the sleepers) of the rail. The second one is called the submodel which is extracted from the global model using the submodelling technique in Abaqus. Time dependent boundary condition was implemented to connect both models.

3.1.1.1 Global model (GM)

The global model consists of one wheel and the rail. This model uses a relatively coarse mesh to obtain results. The submodel is driven by the data from the output database that is generated by the global model. The main target of the global model in this analysis is to drive the boundary conditions for the submodel analysis.

The solution process in this model consists of three steps.

Initial step: In this step the interaction is initiated between the wheel and rail surface

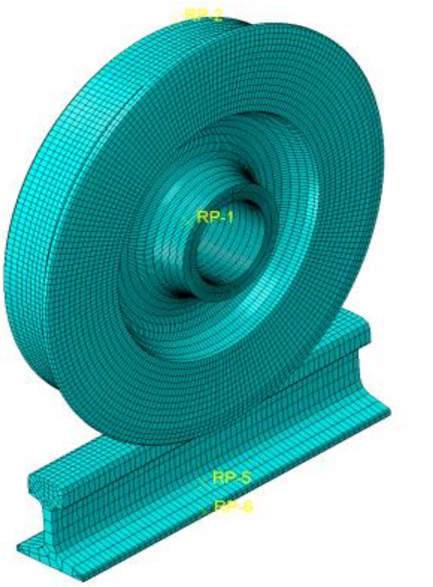

Figure 3-4 Global Model

Step 1: This step is a stabilization step which introduces gradual loading application at the axle point to avoid diverging, bouncing back and numerical instability. In this step the contact between the wheel and the rail is established, concentrated load at a reference point in the wheel center was applied, field outputs are requested and most boundary conditions are created. The step time was given 0.001 s.

Step 2: The wheel was allowed to roll along the track for 600mm, with a translational velocity of 70km/hr (the maximum track speed) and rotational velocity of 64.38rad/s.

The rotational velocity is calculated from:

$$\boldsymbol{\omega} = {}^{\boldsymbol{V}}\!/_{\boldsymbol{W_r}} \qquad 3\text{-}1$$

Where ω is the rotational speed, V is the translational velocity and Wr is the wheel radius at the point of contact.

The step time for the second step (t2) is calculated using the rolling distance (L) and the translational velocity (V) which is, $t_2 = {}^{L}/_{V} = {}^{0.6m}/_{19.44m/s} = 0.03\ s$

Step 3: The load was removed from the wheel

3.1.1.2 Submodel (SM)

The submodel was required to perform more accurate analysis of the contact stresses near contact patches with quite fine meshes because using finer meshes in the global model will result in great deal of computational cost and time. Both models were connected together using time dependent boundary conditions. In submodel one the stress field, contact pressure von-mises stress and shear stress will be determined with acceptable accuracy. Whereas, in submodel two the initiation crack plane and fatigue life are predicted.

Each cycle in this analysis consists of four steps.

Step 1: the load was applied, and wheel/rail contact was established.

Step 2: the wheel is allowed to rotate along the track with scaled distance by applying the same translational and rotational velocity as the global model.

Step 3: the gravity load was removed from the wheel

Step 4: the system is allowed to return to its initial position.

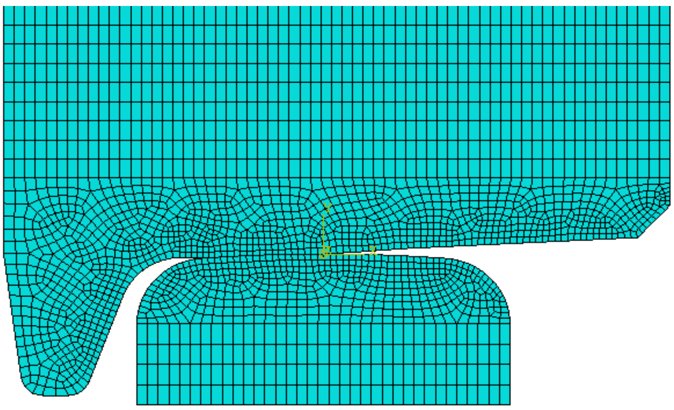

Figure 3-5 Submodel

Modelling dynamic wheel-rail Interaction:

There are three main methods for rail bedding constraints

1. Simply fixed bedding

2. Rigid constraint with one spring-damper (S/D) element

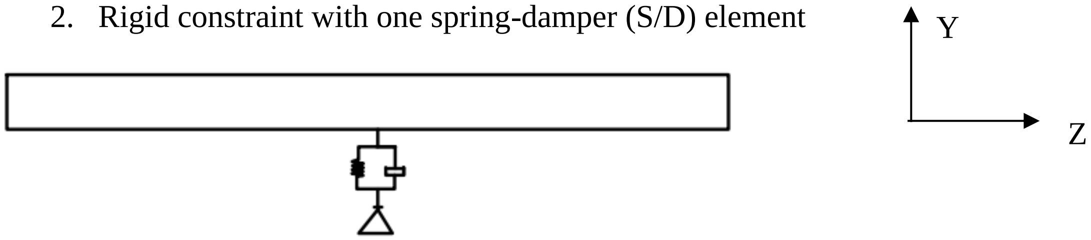

3. Multiple S/D elements for every sleeper

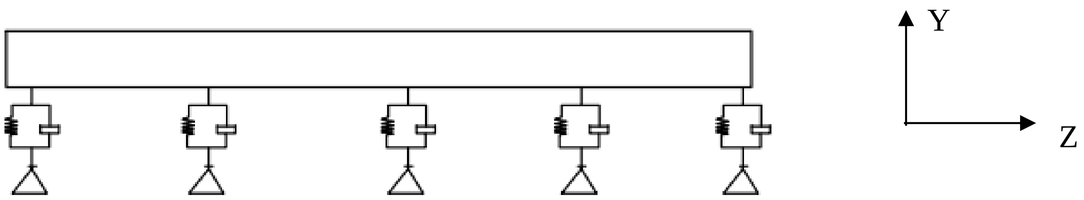

Figure 3-6 Interaction Model

The multiple S/D element method gives the most accurate result at an expense of high computational time. Using rigid constraint with one S/D element provides an acceptable accuracy with lower computational time. Therefore, due to the limitations in computational capability the second method was implemented.

The whole interaction model from bogie to sleeper can be modelled in simplified way as shown in Figure 3-7:

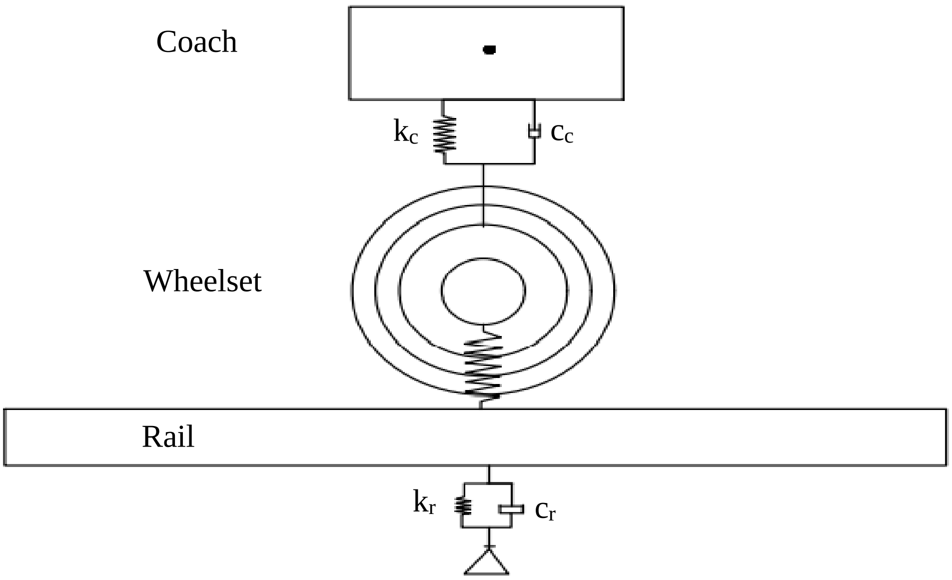

Figure 3-7 Dynamic interaction model

A reference point (pilot node) was created at the center of the axle joint hole and was used to create multi-point constraint (MPC) beam constraint between the internal surface of the hole. The second MPC beam constraint was created between rail bottom surface and a reference point created at the center of this surface.

A concentrated load consisting of the sum of the weight of train body, the passengers and the axle was applied at the reference node created at the center of the axle joint hole.

3.1.1.3 Numerical approach of wheel-rail contact

A finite element code – capable of treating contact problems – should include the following steps: contact detection, construction and update of "contact elements", their incorporation in associated residual vectors and tangential matrices and finally resolution of the resulting problem[28].

Contact detection:

Contact elements are a sort of "bridge elements" between locally separated but potentially interacting bodies. Each contact element contains components (nodes, edges, faces) of both surfaces; the composition of these components depends upon the contact discretization method. The aim of contact detection is to create contact elements containing the proximal components of both surfaces that may come into contact during the current solution step. Contact detection depends on the type of contact discretization.

Contact resolution

Besides structural degree of freedom, contact element may have their proper degree of freedom. These unknowns and the structure of the residual vector and the tangential matrix are evaluated by the resolution method.

Contact discretization

The structure of contact elements that transfer loads from one contacting surface to another is predetermined by contact discretization. Three types of discretization are identified:

1. *Node to Node (NTN)*

This type of discretization introduces limitations on mesh generations and does not allow any finite sliding or large deformations and node to node misalignment. However, it passes the contact patch test – contact pressure is transferred correctly through the conforming contact interface. NTN discretization can be applied to linear and quadratic elements in 2D case and linear elements in 3D case.

2. *Node to Surface (NTS)*

This technique is valid for non-conforming meshes and large deformations or finite sliding. However, it doesn’t pass contact patch test for non-conforming meshes - a uniform contact pressure cannot be transferred correctly through the contact interface. So, some modification might be needed.

3. *Surface to Surface (STS)*

STS discretization technique has been efficiently implemented to two- and three-dimensional problems coupled with the mortar method for non-conforming meshes.

In the current study, Wheel/rail contact was defined using surface to surface discretization method. This is because surface to surface approach has many benefits over the node-to-node approach such as[28]:

- reduces likelihood of large localized penetrations

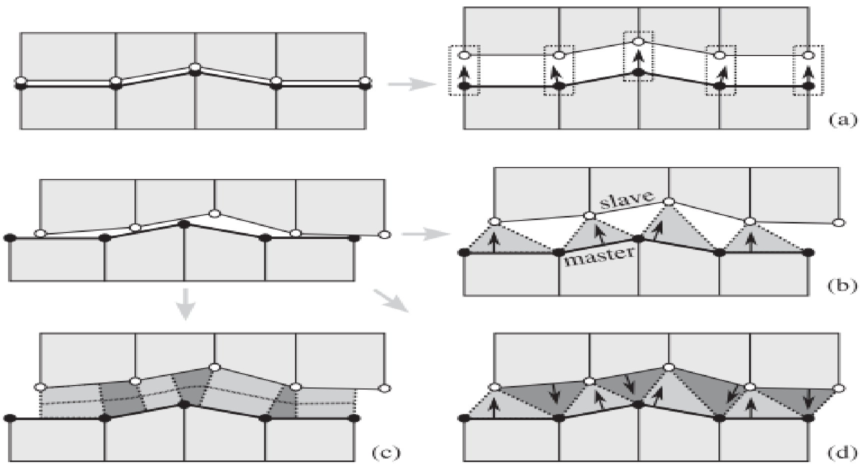

Figure 3-8 Graphical representation of different contact discretization: for small deformations/sliding (a) node-to-node, associated pairs of nodes and normals; for large deformations/slidings (b) node-to-segment, slave nodes and associated master segment

- decreases sensitivity of results to master and slave roles and node alignment
- provides more accurate contact stress results
- has better convergence

In the contact property section, penalty friction formulation was applied to the model to enforce the contact constraints.

Relative sliding formulation

Abaqus offers finite- and small-sliding versions of S-to-S and N-to-S contact formulations. *Small sliding formulation* assumes relative motion per slave node remains small compared to local curvature of the master surface and facet size of the master surface. This formulation has a potential for reduced cost per iteration and finding a converged solution in fewer iterations. However, results obtained can be non-physical if relative tangential motion does not remain small [15]. *Finite sliding formulation* is appropriate for this study to accurately represent the problem. Coefficient of friction of 0.3 was used, accounting the lubrication. Coulomb's friction law (Equation 3-6) was used to describe to describe frictional rolling contact. In addition to this, in this study, the initial contact point is assumed to occur at the rail head center and wheel tread center Figure 3-2.

$$\boldsymbol{\tau_{lim}} = \boldsymbol{\mu P_{o,}} \ \|\boldsymbol{\tau}\| = \boldsymbol{\tau_{lim}} \qquad \textbf{3-2}$$

Where $P_{o,}$ is the maximum contact pressure; μ is the friction coefficient; τ_{lim} is the limiting frictional stress; τ is the frictional stress.

Boundary conditions (constraints):

Two amplitudes were created. Amplitude-1 is used for every boundary condition with gradual increase of magnitude to avoid divergence error by eliminating sudden increase of movement and loading.

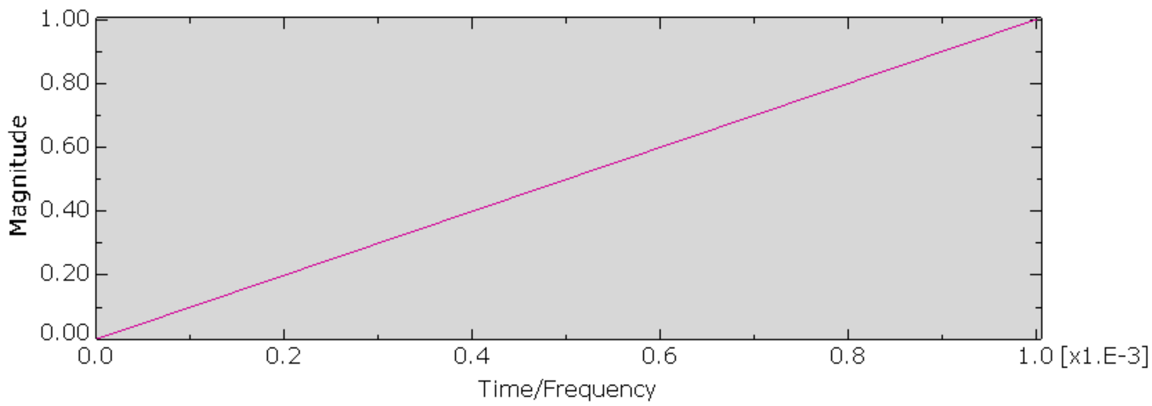

Figure 3-9 Amplitude 1

Amplitude-2 is for the loading and represents smooth increase of the concentrated load in the first step (stabilization step) and constant magnitude throughout the second step (rolling step).

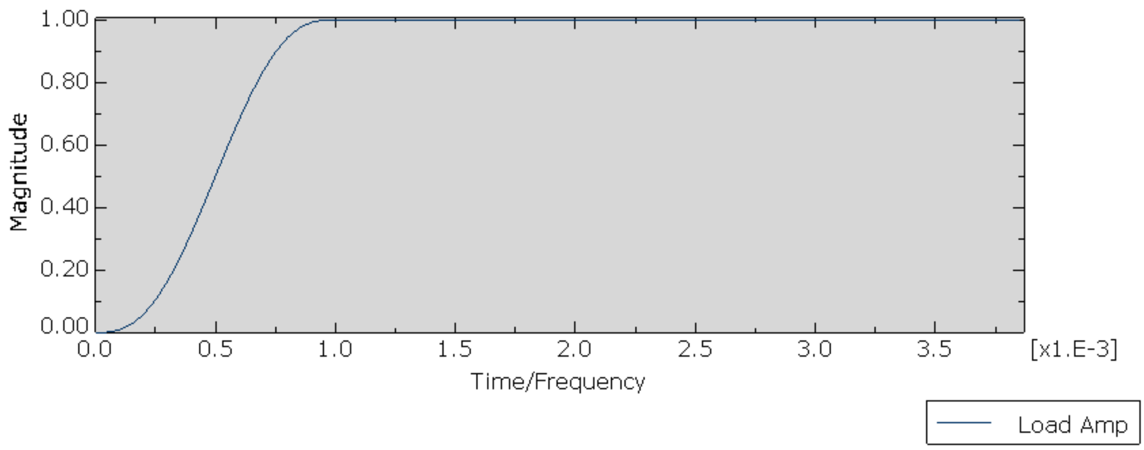

Figure 3-10 Amplitude 2

Discretization

Coarse and fine mesh: The global model uses coarse meshes compared to the submodel because we only need the global model to extract the boundary conditions at the cut section in the submodel. Moreover, the use of the submodel can save up to more than 100 times computational time [14]. The submodel (section of the global model) only takes account for the geometry near the area of contact. Therefore, finer meshes are applied for the submodel. The stress and strain results for the two models need not be the same. Wide difference in element size between the two models accounts for the divergence in the numerical results. Generally, relatively even finer meshes are applied in areas of contact between the wheel and the rail to get more accurate numerical results.

Element type and element size. The element type used for the global and the submodel is a fully integrated eight-node linear brick (C3D8) elements.

3.1.1.4 Convergence analysis.

In the submodel, higher level of accuracy is required at the lower wheel section and the upper rail part (rail head zone) where several strains and stresses are anticipated with reasonable computational time. As a result, mesh sensitivity analysis needs to be performed to determine the optimum mesh size. Mesh refinement is carried out only at lower wheel part and the upper rail part. Various element sizes were taken and the element size where numerical results start converging was implemented to conduct the rest of the analysis.

The element sizes of $1.2\ mm, 1.4\ mm, 1.6\ mm, 1.8\ mm, 2.0\ mm\ and\ 3.0mm$ are used. The highest contact pressure was obtained at element sizes between $1.2\ mm\ and\ 1.8\ mm$, whereas the lowest was obtained at $3.0mm$ element size. This implies, the finer the mesh the higher the numerical results will be. The variation in result with in the element size range between 1.2 mm and 1.8 mm is less than 1.8%. Therefore, we can get a result with an acceptable accuracy and much lower computational effort at mesh size 1.8 mm x 1.8 mm. So, 1.8mm element size was used for the rest of the analysis.

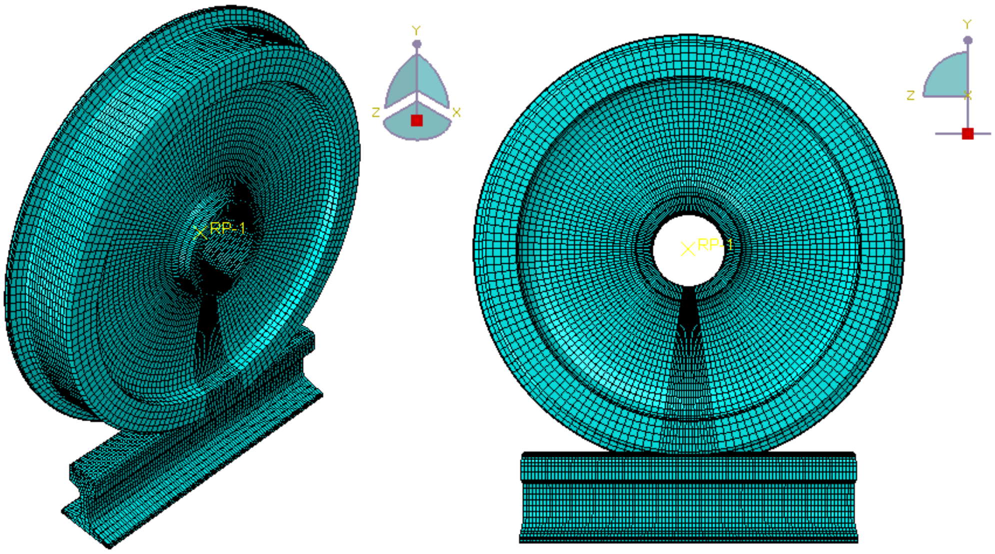

Figure 3-11 Mesh of Wheel-rail assembly in Abaqus CAE

Table 3-2 Mesh Convergence

Element size	Von-mises stress (MPa)
$3.0mm$	520
$2.0mm$	537
$1.8mm$	550
$1.6mm$	540
$1.4mm$	543
$1.2mm$	545

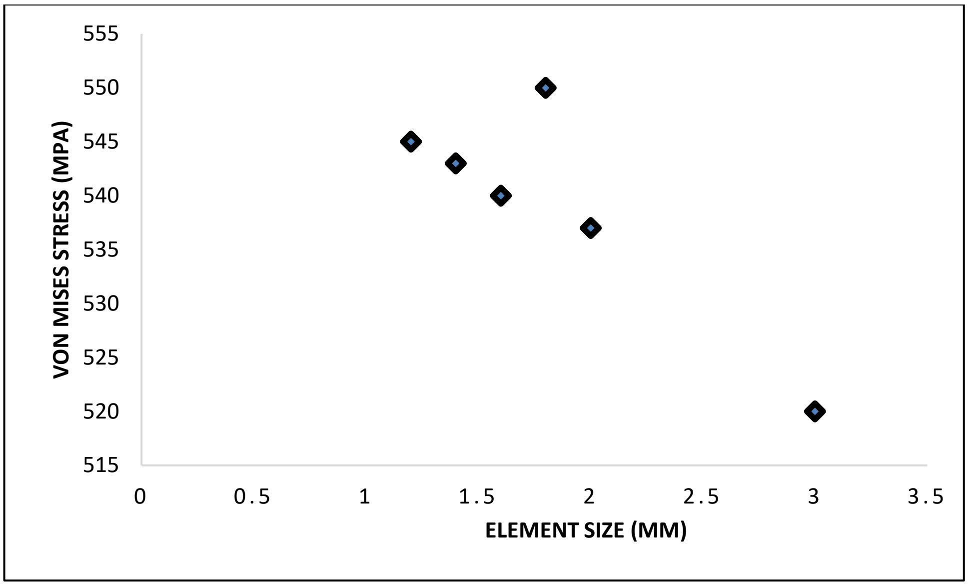

Figure 3-12 Convergence plot

3.2 Materials model

In this section of the paper, first the material properties of the wheel and the rail and the loading conditions of the rail stock are presented. The material response at the wheel-rail contact region over cyclic loading is also thoroughly studied. For example, there are four possible ways the material at wheel-rail contact region might respond; Perfectly elastic, elastic shakedown, plastic shakedown and ratcheting responses. The loading condition, material hardening, and the variation of contact conditions due to wear and/or plastic deformation are major factors in deciding in which way the material might respond.

3.2.1 Wheel and rail material model

In this paper, standard wheel and rail materials models are implemented to conduct the analysis.

Table 3-3 Chemical composition [29]

	C%	Si%	Mn%	Po%	S%	Cr%	Co%	Mb%	Ni%
R8T	0.54	0.36	0.80	0.02	0.006	0.30	0.30	0.08	0.14

Table 3-4 Mechanical properties of wheel [30]

Wheel type	Tensile strength (MPa)	Yield strength (MPa)	Elastic modulus (GPa)	Poisson's ratio
R8T	980	540	206	0.29

Table 3-5 Mechanical properties of rail

Rail type	Tensile strength (MPa)	Yield strength (MPa)	Elastic modulus (GPa)	Poison's ratio
50kg/m	960-980	543	210	0.3

Table 3-6 Loading conditions of R8T wheel

Loading condition	**Axle load (KN)**
L1	110
L2	140
L3	160
L4	180
L5	200
L6	220

3.2.2 Material Response

Repeated rolling or sliding contacts stresses the material cyclically. Dependent on the character and intensity of applied contact loads, the material hardening and the variation of contact conditions due to plastic deformation and wear, the material in wheel-rail contact region responds in one of the following four ways [4], [15], [16].

a. Perfectly elastic behavior if the contact load is sufficiently low and does not exceed the elastic limit and the material is purely elastic and reversible, i.e. for a line contact p_{max}/τ_c= 0.31 or expressed in the load intensity τ_c/p_{max}=1/0.31. This response is rare to occur in wheel-rail contact zones.
b. Elastic shakedown behavior, in which contact load exceeds the elastic limit and plastic deformation takes place during running in. However, after some cycles,

residual stresses or strain hardening shakedown the material response to perfectly elastic state.

c.

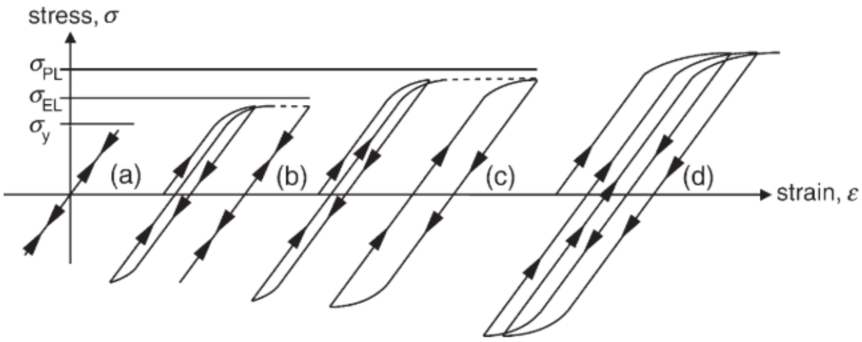

Figure 3-13 Illustration of different material responses to cyclic loading: (a) depicts perfectly elastic; (b) elastic shakedown; (c) plastic shakedown; (d) ratchetting [8]

d. Plastic shakedown behavior, in which the steady state is a closed elastic plastic loop, with no net strain (plastic deformation) accumulation.
e. Ratcheting behavior, the steady state is an open elastic plastic loop, there is an accumulation of a net strain at every cycle until the material ductility is exhausted.

In the analysis of the wheel-rail contact the material models should be defined properly to get accurate results that represent the real scenario. Among this is the material property after yielding had occurred.

Elasticity. Elastic properties are applied for the entire global model and for the regions outside the vicinity of contact area in the submodel.

Plasticity. Multiaxial Cyclic plastic deformation occurs in rolling contact fatigues like the wheel-rail contact. Regions in vicinity of contact are assumed to undergo plastic deformation. The plastic zone is taken to extend 15 mm along the depth of the wheel [15] (the red section shown in Figure 3-14).

The basic elements of plasticity theory consist of:

Yield function: determines when plastic flow initiates.

Flow rule: relates the applied stress increments to the resulting plastic strain increments once plastic flow has initiated. Constitutive equations are used to relate the stresses and the plastic strains.

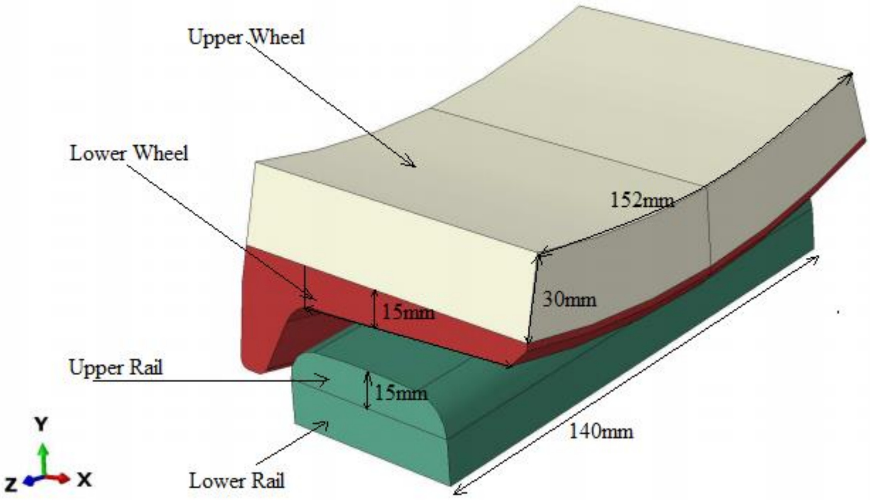

Figure 3-14 Elastic and plastic behavior assignment for wheel sections

Hardening rule: describes the change in the yield criterion as a function of plastic strains. One possible hardening rule is the *isotropic rule*, which assumes that strain hardening corresponds to an enlargement of the yield surface (i.e., an increase in Sy) without change of shape or position in the stress space. Another is the *kinematic rule*, which assumes that strain hardening shifts the yield surface without changing its size or shape [31].

Different constitutive models can be used to accurately capture the effect of cyclic loading in rolling contact stress analysis, such as linear kinematic hardening model [14] or non-linear kinematic hardening model [15]. Non-Linear isotropic/kinematic hardening model (combined) proposed by Chaboche and Lemaitre is adopted in this study due to its ability to reproduce phenomenon like ratcheting and cyclic hardening [4], [15], [16].

$$\dot{\alpha}_k = C_k \frac{1}{\sigma_o}(\sigma - \alpha)\dot{\bar{\varepsilon}}^p - \gamma_k \alpha_k \dot{\bar{\varepsilon}}^p, \quad (k = 1, 2, 3) \tag{3-3}$$

$$\sigma_y = \sigma_o + Q\left(1 - e^{-R\bar{\varepsilon}^p}\right) \tag{3-4}$$

Where α is the back-stress tensor which designates the translation of the yield surface in the stress space; σ is the stress tensor; $\dot{\bar{\varepsilon}}^p$ is the plastic strain rate; $\bar{\varepsilon}^p$ is the plastic strain; σ_o is the initial yield stress at zero plastic strain; σ_y is the yield stress; C_k, γ_k R, Q are material parameters calibrated from uniaxial test data.

The material models for both the wheel and the rail were inserted to the analysis according to Table 3-7. They are taken from [26], [31], [32] for **R8T** wheel.

Table 3-7 Material parameter for the R8T wheel

Parameters	$E(GPa)$	ν	$\sigma_o(MPa)$	R	$Q(MPa)$	C_k	γ_k
Values	206	0.29	543	0.47	22.8	6490	0.81

Since the there is a considerable increase in temperature at contact region between the wheel and the rail, it is tried to incorporate the effect of the temperature on the elastic modulus of the material. The temperature in the wheel/rail contact region can be as high as 200ºC [32][33].

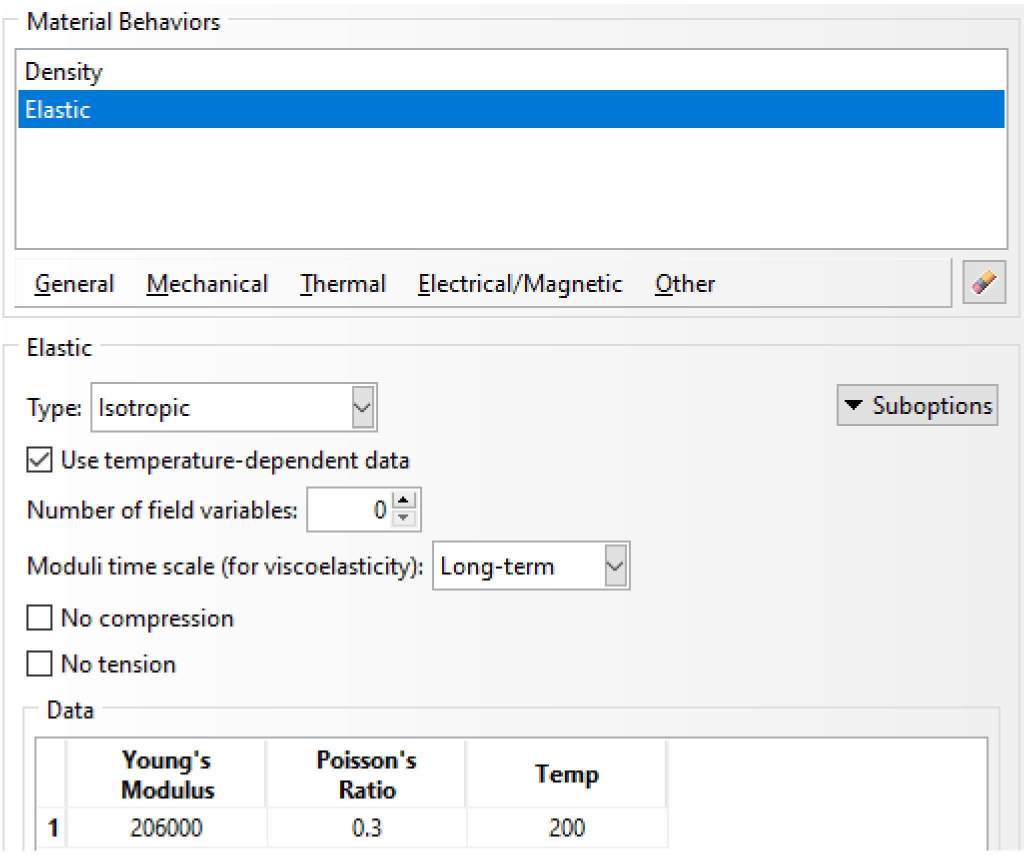

Figure 3-15 Elastic Data on *Abaqus 2020*

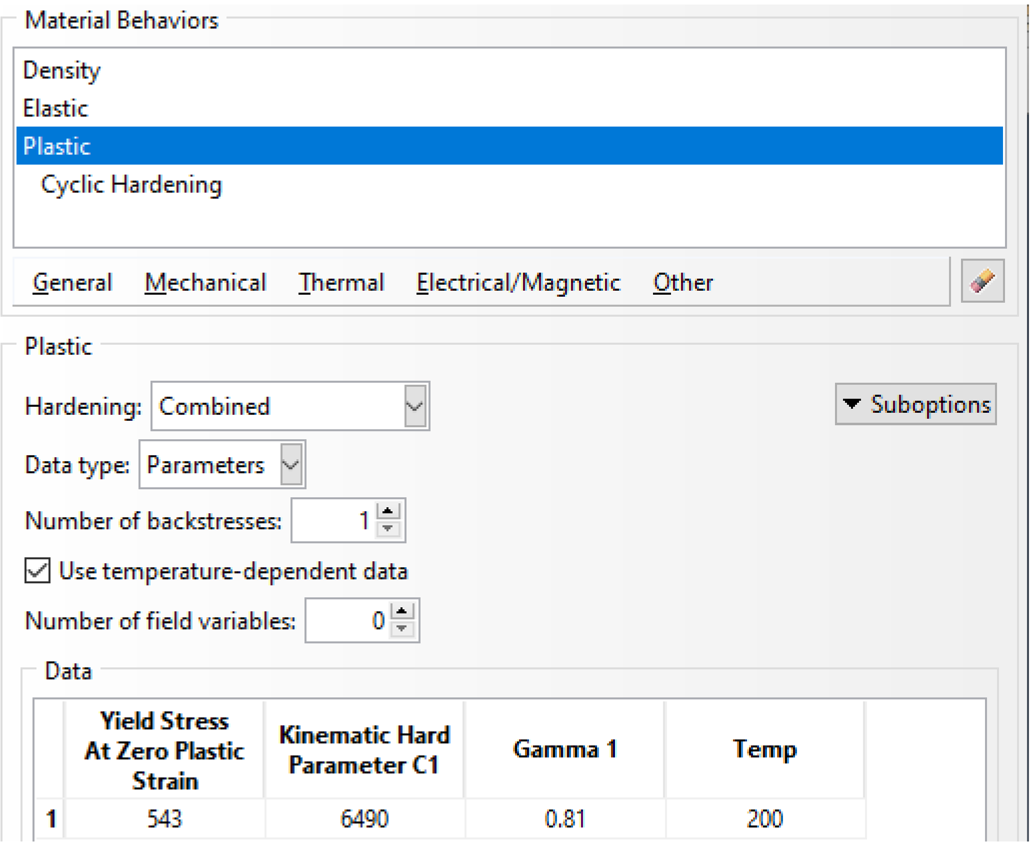

Figure 3-16 Plastic data on *Abaqus 2020*

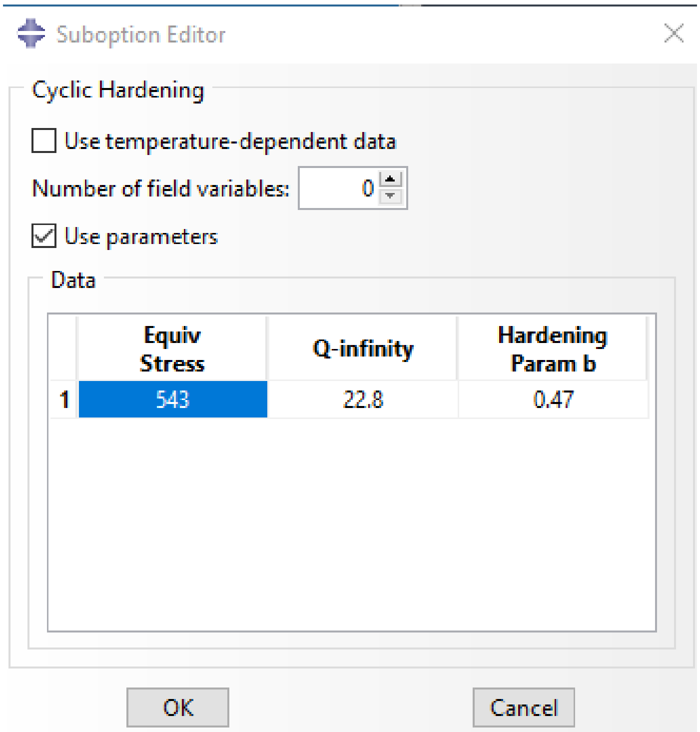

Figure 3-17 Cyclic Hardening

3.3 Rolling Contact Fatigue Model

Two types of approaches may be used in analyses of fatigue crack initiation: (1) the defect-tolerant approaches, and (2) the total-life approaches. The defect-tolerant approaches rely on the resistance to crack growth in materials that are inherently flawed by small cracks. These approaches use fracture mechanics to calculate the number of cycles required to propagate a crack to a critical size.

The total-life approaches estimate the resistance to fatigue crack initiation based on nominally defect-free materials and components. These approaches attempt to analyze the total fatigue life to failure (crack initiation); they are classified into stress-based, strain-based and energy-based approaches. The stress-based approach is mostly applied to low cyclic stress ranges that are designed against fatigue crack initiation (high-cycle fatigue failures)[25]. The strain-based approach, also called the strain-life approach, involves the fatigue life prediction of crack initiation according to which the strain range characterizes the fatigue life.

In this paper strain-based approach is adopted because the stresses between the wheel and the rail are high enough to cause plastic deformations (strains). As a result, strains are more likely govern failures due to fatigue.

3.3.1 Critical Plane Approaches

Critical plane models are found more suitable than bulk fatigue damage models as they showed better consistency with experiments and can predict the location and orientation of damage (crack initiation).

Limitation of many critical plane-based criterion reviewed in previous sections lies in handling of compressive mean stresses and handling of non-proportional loading where the maximum normal stress and the maximum shear stress in the cycle does not coincide.

However, among these models critical plane model proposed by Jiang and Sehitogelu and Liu accounted for these limitations and showed good agreement with rolling contact fatigue experimental results [4], [8], [22]–[26], [32]. Besides, these models can be used for both elastic shakedown (HCF) and plastic shakedown (LCF) material responses [10]. It was not possible to implement the Liu’s criteria in this paper because it uses large number of material parameters only available for few materials and require experiments to be determined.

3.3.2 Jiang-Sehitogelu Criterion

Jiang and Sehitogelu defined the damage parameter as, [23].

$$\boldsymbol{FP} = \langle \boldsymbol{\sigma_{max}} \rangle \frac{\Delta\epsilon}{\mathbf{2}} + \boldsymbol{J}\Delta\boldsymbol{\tau}\Delta\boldsymbol{\gamma} \qquad \textbf{3-5}$$

The critical plane is a plane with maximum fatigue parameter. After the critical plane is determined the number of cycles to crack initiation is obtained from as shown in chapter 2:

$$\boldsymbol{FP_{max}} = \begin{cases} \frac{(\sigma'_f)^2}{E}(\mathbf{2}\boldsymbol{N_f})^{\mathbf{2}\boldsymbol{b}} + \boldsymbol{\sigma'_f}\boldsymbol{\epsilon'_f}(\mathbf{2}\boldsymbol{N_f})^{\boldsymbol{b}+\boldsymbol{c}} \\ \frac{(\tau'_f)^2}{G}(\mathbf{2}\boldsymbol{N_f})^{\mathbf{2}\boldsymbol{b}} + \boldsymbol{\tau'_f}\boldsymbol{\gamma'_f}(\mathbf{2}\boldsymbol{N_f})^{\boldsymbol{b}+\boldsymbol{c}} \end{cases} \qquad \textbf{3-6}$$

The first form is used for mode-1 (tensile dominated) crack and the latter is for mode-2 (shear dominated) crack initiation.

3.3.3 Critical Plane Search (CPS)

Proportional loading. In this type of loading the maximum normal stress and the maximum shear stress coincide with each other. Besides, when loading is proportional, the principal stresses do not change direction during the loading cycle, making it easy to calculate the maximum shear stress amplitude [35].

Non-proportional loading. In this type of loading the maximum shear stress and the maximum normal stress do not coincide. When the shear stress reaches maximum, the normal stress reaches its minimum and vice versa [35]. As a result, the principal directions of the alternating stresses are not fixed, but change orientation during this type of loading, making it difficult to calculate the maximum shear stress amplitude. We can see from stress history curve in Figure 3-18 that the loading is non-proportional in our wheel- rail interaction problem.

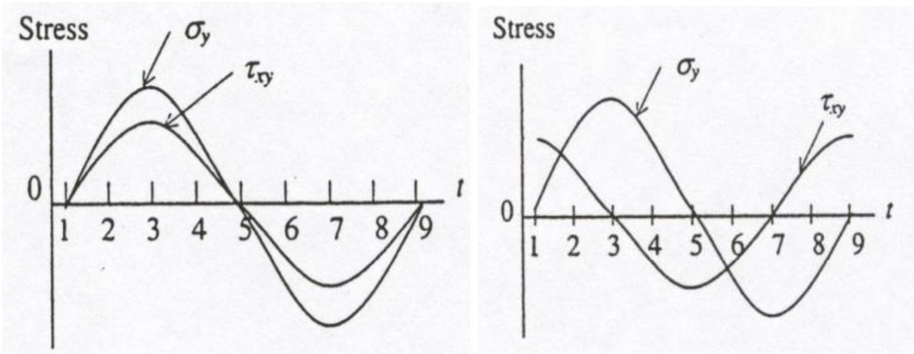

Figure 3-18 Stress and strain history curve for proportional (left) and non-proportional (right) loading

According to Jiang and Sehitogelu the crack plane with orientation θ is defined by:

$$\max_{\theta}\left[\langle\sigma_{max}\rangle\frac{\Delta\epsilon}{2}+J\Delta\tau\Delta\gamma\right] \quad \textbf{3-7}$$

The critical plane θ is the plane with maximum fatigue parameter, FP max. Therefore, every angle θ is searched for with in a range [0, π] using θ increment of 1^0. The most critical point at depth d suffering from maximum von-mises stresses is taken for calculations.

The normal and shear stresses and strain at an arbitrary plane θ is defined using stress transformation equations as [36], [37]:

3.3.3.1 Two-dimensional CPS

In the consideration location of the plane is identified using a single angle θ in the two-dimensional Y-Z plane. Two-dimensional stress and strain transformation equations (3-8 to 3-11) are used [37] to determine the crack angle. The depth d is determined by exploring all the possible nodes in the radial section of the wheel for maximum fatigue parameter[14]. Some papers assume the depth, d of maximum damage is where von-mises stress is maximum[15]. In this paper, it is proven that both approaches yield the same result.

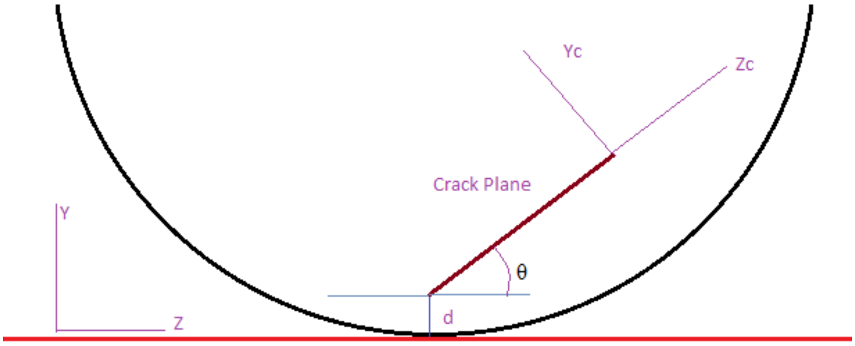

Figure 3-19 Location of critical plane

$$\boldsymbol{\sigma_\theta} = \frac{\sigma_z+\sigma_y}{2} + \frac{\sigma_z+\sigma_y}{2}\boldsymbol{cos}(2\theta) + \tau_{yz}\,\boldsymbol{sin}(2\theta) \quad \textbf{3-8}$$

$$\boldsymbol{\tau_\theta} = \frac{\sigma_z-\sigma_y}{2}\boldsymbol{sin}(2\theta) - \tau_{yz}\,\boldsymbol{cos}(2\theta) \quad \textbf{3-9}$$

$$\boldsymbol{\epsilon_\theta} = \frac{\epsilon_z+\epsilon_y}{2} + \frac{\epsilon_z+\epsilon_y}{2}\boldsymbol{cos}(2\theta) + \frac{\gamma_{yz}}{2}\boldsymbol{sin}(2\theta) \quad \textbf{3-10}$$

$$\boldsymbol{\gamma_\theta} = -(\epsilon_z - \epsilon_y)\,\boldsymbol{sin}(2\theta) + \gamma_{yz}\,\boldsymbol{cos}(2\theta) \quad \textbf{3-11}$$

3.3.3.2 Three-dimensional CPS

The location of the critical plane can be defined by two spherical coordinates θ and φ and the stress and strain on an arbitrary plane (with new coordinate X Y Z) can be calculated using three-dimensional stress and strain transformation equations below [37]:

Table 3-8 Direction cosines

	x	y	z
X	$l_1 = \cos\varphi\sin\theta$	$m_1 = \sin\varphi\cos\theta$	$n_1 = \cos\theta$
Y	$l_2 = -\sin\varphi$	$m_2 = \cos\varphi$	$n_2 = 0$
Z	$l_3 = -\cos\varphi\cos\theta$	$m_3 = -\sin\varphi\cos\theta$	$n_3 = \sin\theta$

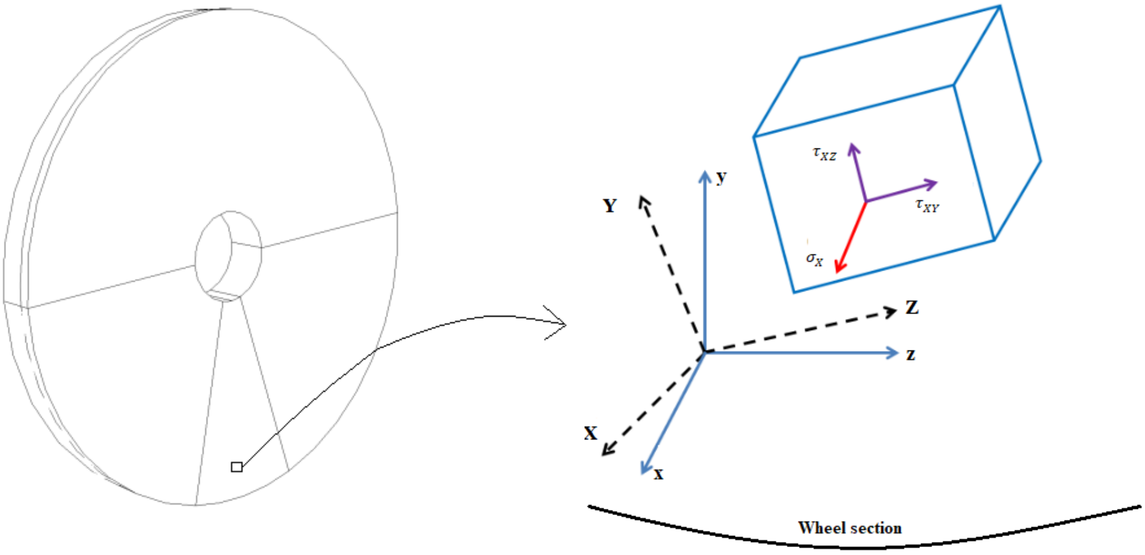

Figure 3-20 A stress element and its stress state in the wheel at a rotated coordinate axis

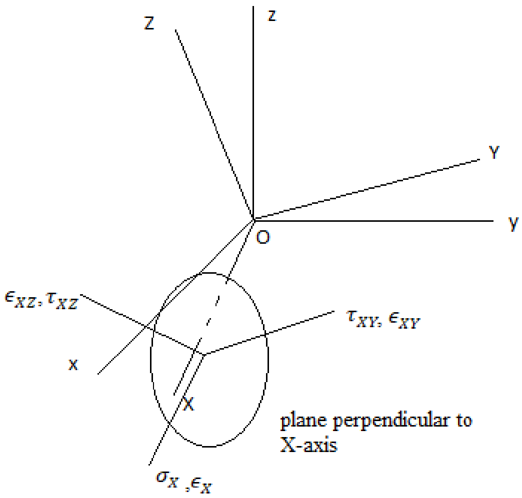

Figure 3-21 A stress state at an arbitrary plane

Stress transformation equations

Normal stress,

$$\sigma_X = {l_1}^2\sigma_x + {m_1}^2\sigma_y + {n_1}^2\sigma_z + 2m_1n_1\tau_{yz} + 2l_1n_1\tau_{xz} + 2l_1m_1\tau_{xy} \tag{3-12}$$

$$\sigma_Y = {l_1}^2\sigma_x + {m_1}^2\sigma_y + {n_1}^2\sigma_z + 2m_1n_1\tau_{yz} + 2l_1n_1\tau_{xz} + 2l_1m_1\tau_{xy} \tag{3-13}$$

$$\sigma_Z = {l_1}^2\sigma_x + {m_1}^2\sigma_y + {n_1}^2\sigma_z + 2m_1n_1\tau_{yz} + 2l_1n_1\tau_{xz} + 2l_1m_1\tau_{xy} \tag{3-14}$$

Shear stress,

$$\tau_{XZ} = l_1l_3\sigma_x + m_1m_3\sigma_y + n_1n_3\sigma_z + (m_1n_3 + m_3n_1)\tau_{yz} + (l_1n_3 + l_3n_1)\sigma_x + (l_1m_3 + l_3m_1)\tau_{xy} \tag{3-15}$$

$$\tau_{XY} = l_1l_2\sigma_x + m_1m_2\sigma_y + n_1n_2\sigma_z + (m_1n_2 + m_2n_1)\tau_{yz} + (l_1n_2 + l_2n_1)\sigma_x + (l_1m_2 + l_2m_1)\tau_{xy} \tag{3-16}$$

$$\tau_{YZ} = l_2l_3\sigma_x + m_2m_3\sigma_y + n_2n_3\sigma_z + (m_2n_3 + m_3n_2)\tau_{yz} + (l_2n_3 + l_3n_2)\sigma_x + (l_2m_3 + l_3m_2)\tau_{xy} \tag{3-17}$$

Strain transformation equations

Normal strains,

$$\epsilon_X = {l_1}^2\epsilon_x + {m_1}^2\epsilon_y + {n_1}^2\epsilon_z + 2m_1n_1\epsilon_{yz} + 2l_1n_1\epsilon_{xz} + 2l_1m_1\epsilon_{xy} \tag{3-18}$$

$$\epsilon_Y = {l_2}^2\epsilon_x + {m_2}^2\epsilon_y + {n_2}^2\epsilon_z + 2m_2n_2\epsilon_{yz} + 2l_2n_2\epsilon_{xz} + 2l_2m_2\epsilon_{xy} \tag{3-19}$$

$$\epsilon_Z = {l_3}^2\epsilon_x + {m_3}^2\epsilon_y + {n_3}^2\epsilon_z + 2m_3n_3\epsilon_{yz} + 2l_3n_3\epsilon_{xz} + 2l_3m_3\epsilon_{xy} \tag{3-20}$$

Shear strains,

$$\boldsymbol{\epsilon_{XZ} = l_1 l_3 \epsilon_x + m_1 m_3 \epsilon_y + n_1 n_3 \epsilon_z + (m_1 n_3 + m_3 n_1)\epsilon_{yz} + (l_1 n_3 + l_3 n_1)\epsilon_x + (l_1 m_3 + l_3 m_1)\epsilon_{xy}} \quad \textbf{3-21}$$

$$\boldsymbol{\epsilon_{XY} = l_1 l_2 \epsilon_x + m_1 m_2 \epsilon_y + n_1 n_2 \epsilon_z + (m_1 n_2 + m_2 n_1)\epsilon_{yz} + (l_1 n_2 + l_2 n_1)\epsilon_x + (l_1 m_2 + l_2 m_1)\epsilon_{xy}} \quad \textbf{3-22}$$

$$\boldsymbol{\epsilon_{YZ} = l_2 l_3 \epsilon_x + m_2 m_3 \epsilon_y + n_2 n_3 \epsilon_z + (m_2 n_3 + m_3 n_2)\epsilon_{yz} + (l_2 n_3 + l_3 n_2)\epsilon_x + (l_2 m_3 + l_3 m_2)\epsilon_{xy}} \quad \textbf{3-23}$$

For a point at wheel the load varies with time due the rotation of the wheel. Therefore, the stress state at a point can be expressed as the Cauchy stress and strain tenor (stress and strain history output), as shown below:

$$\boldsymbol{\sigma(t) = \begin{bmatrix} \sigma_X(t) & \tau_{XY(t)} & \tau_{XZ}(t) \\ \tau_{XY}(t) & \sigma_Y(t) & \tau_{YZ}(t) \\ \tau_{XZ}(t) & \tau_{YZ}(t) & \sigma_Z(t) \end{bmatrix}} \quad \textbf{3-24}$$

And similarly, for the strain,

$$\boldsymbol{\epsilon(t) = \begin{bmatrix} \epsilon_X(t) & \epsilon_{XY(t)} & \epsilon_{XZ}(t) \\ \epsilon_{XY}(t) & \epsilon_Y(t) & \epsilon_{YZ}(t) \\ \epsilon_{XZ}(t) & \epsilon_{YZ}(t) & \epsilon_Z(t) \end{bmatrix}} \quad \textbf{3-25}$$

The discrete values of history outputs, $\sigma(t)$ and $\epsilon(t)$, can be obtained from the finite element model analysis at each load step at a point in the wheel which has suffered the maximum von-mises stress [15]. Hence, the stress and strain transformations are evaluated at each time (load step). Alternatively, for easy input to the algorithm, the stress and strain history results can be approximated using trigonometric functions as follows while the wheel is interacting with the rail [20].

$$\boldsymbol{\sigma_X(t) = \sigma_m + \sigma_a \cos(\omega t)} \quad \textbf{3-26}$$

$$\boldsymbol{\tau_{XY}(t) = \tau_m + \tau_a \sin(\omega t)} \quad \textbf{3-27}$$

σ_m and τ_m are mean stresses and σ_a and τ_a are stress amplitudes.

The same approach is used for the strain history outputs too.

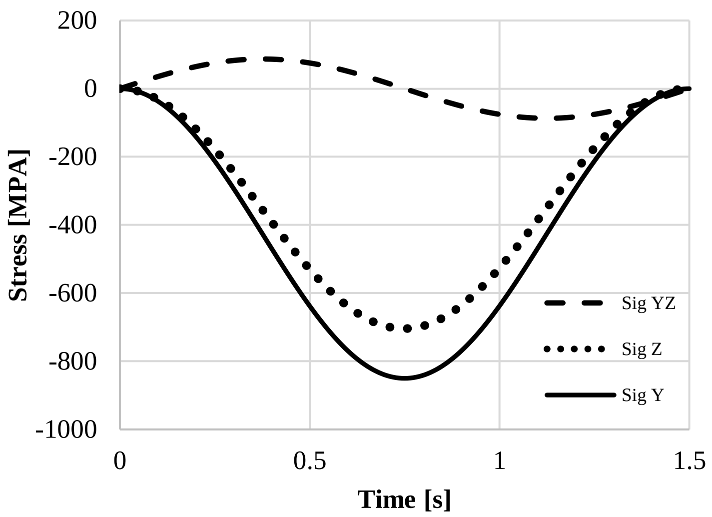

Figure 3-22 Sinusoidal approximation for the non-proportional loading

Recalling the Jiang and Sehitogelu fatigue damage criterion, the damage parameter was defined as, [23].

$$\boldsymbol{FP} = \langle \boldsymbol{\sigma_{max}} \rangle \frac{\Delta\epsilon}{\mathbf{2}} + \boldsymbol{J}\Delta\boldsymbol{\tau}\Delta\boldsymbol{\gamma} \qquad \textbf{3-28}$$

$\Delta\epsilon$ is the normal strain range, $\Delta\epsilon = \epsilon\ (t)_{max} - \epsilon\ (t)_{min}$

$\Delta\gamma$ is the shear strain range, $\Delta\gamma = \gamma(t)_{max} - \gamma(t)_{min}$

$\Delta\tau$ is the shear stress range, $\Delta\tau = \tau(t)_{max} - \tau(t)_{min}$

⇨ $\langle \sigma_{max} \rangle = 0.5(|\sigma_{max}| + \sigma_{max})$

Where, σ_{max} is the maximum normal stress.

The crack plane (the critical plane) is the plane where the damage parameter, FP is maximum. To find this plane every plane should be checked with 1^0 angle increments. However, this process is highly time demanding if tried manually. Therefore, a MATLAB algorithm (Appendix B and C) that checks every plane with in the given increment is developed. The algorithm implements *a nested for-loop* mechanism to iterate every value at every plane.

The algorithm eventually determines the maximum fatigue parameter (FP_{max}) and its orientation. Then FP_{max} is used to calculate the fatigue life N_f according to equation

$$FP_{max} = \begin{cases} \frac{(\sigma'_f)^2}{E}(2N_f)^{2b} + \sigma'_f \epsilon'_f (2N_f)^{b+c} \\ \frac{(\tau'_f)^2}{G}(2N_f)^{2b} + \tau'_f \gamma'_f (2N_f)^{b+c} \end{cases} \tag{3-29}$$

3.3.4 Fatigue life analysis of the wheel

The fatigue analysis is made as a post-process using the results from the FE analysis. In the post-process, the most critical material points and plane for crack initiation (the crack plane) are identified. The crack plane is determined by using a numerical algorithm developed using MATLAB together with a theoretical model for fatigue crack initiation, which gives the most critical material plane with respect to fatigue damage. When the crack plane has been identified, the fatigue life to crack initiation is computed, and the results are compared with previous literatures.

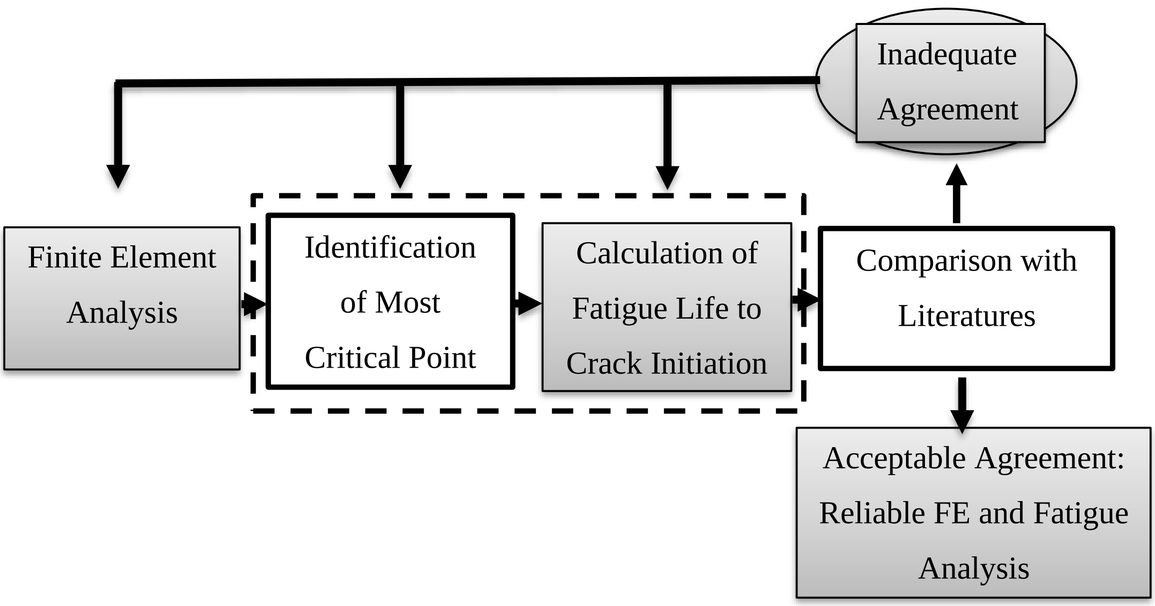

Figure 3-23 A flow diagram presenting a strategy for fatigue life prediction of crack initiation.

3.3.4.1 Calculation of Fatigue Life

Since all the normal stresses are in compression, the shear cracking (Mode II) governs the fatigue parameter and the number of cycles to crack initiation should be evaluated using the shear form equation.

$$FP_{max} = \frac{(\tau'_f)^2}{G}(2N_f)^{2b} + \tau'_f \gamma'_f (2N_f)^{b+c} \tag{3-30}$$

Table 3-9 Mechanical properties of the wheel steel [20]

Parameters	G (GPa)	$\boldsymbol{b}$	$\boldsymbol{c}$	$\boldsymbol{\tau'_f}$(Mpa)	$\boldsymbol{\gamma'_f}$(%)	$\boldsymbol{J}$
Value	80	-0.089	-0.559	468	15.45	0.2

The S-N curve for the life prediction was plotted as follows using shear strain amplitude. The variable S represents the combination of shear strain amplitude.

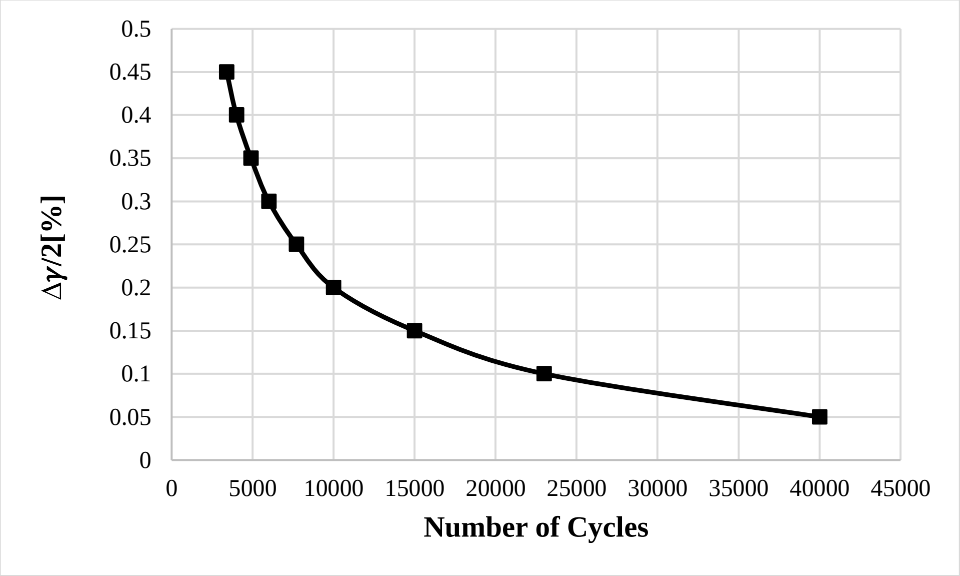

Figure 3-24 S-N Curve

CHAPTER 4 RESULT AND DISCUSSION

4.1 Numerical Example

In this section, a specific example simulating the working conditions of R8T wheel was investigated using the procedures and tools developed by the author.

Table 4-1 Working conditions for the numerical example

Parameters		**Design value**
Train velocity,	V	70 km/hr
Vertical load,	F	160 kN
Friction coefficient,	μ	0.3
Wheel diameter,	2Rw1	660 mm
Wheel radius of curvature,	Rw2	470 mm
Rail radius of curvature,	Rr2	300 mm

4.1.1 Contact pressure distribution

Contact pressure distribution along rolling and lateral directions of the wheel

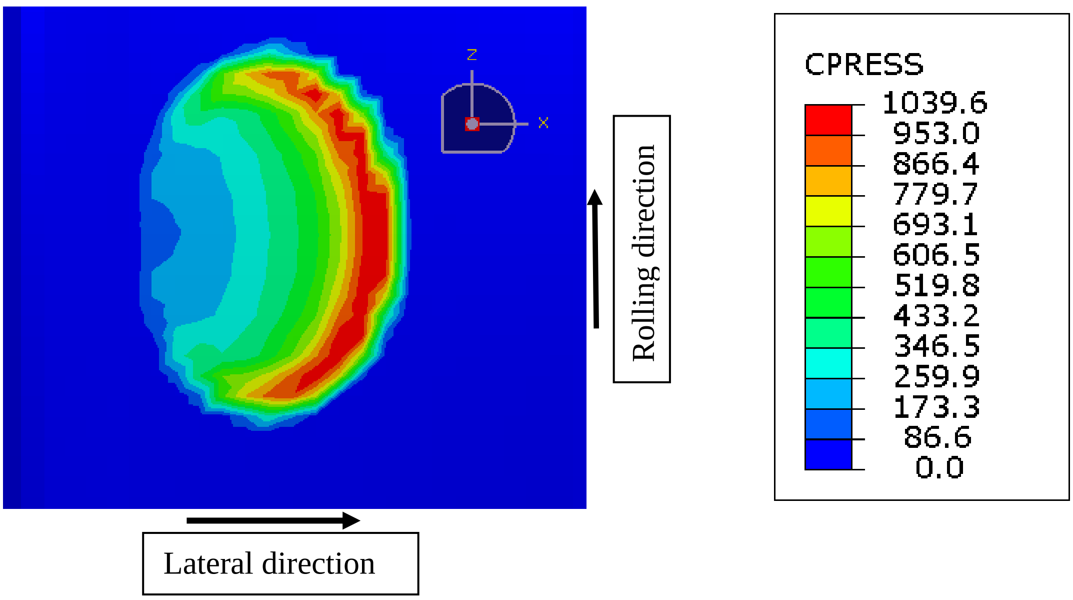

Figure 4-1 Contact Pressure distribution

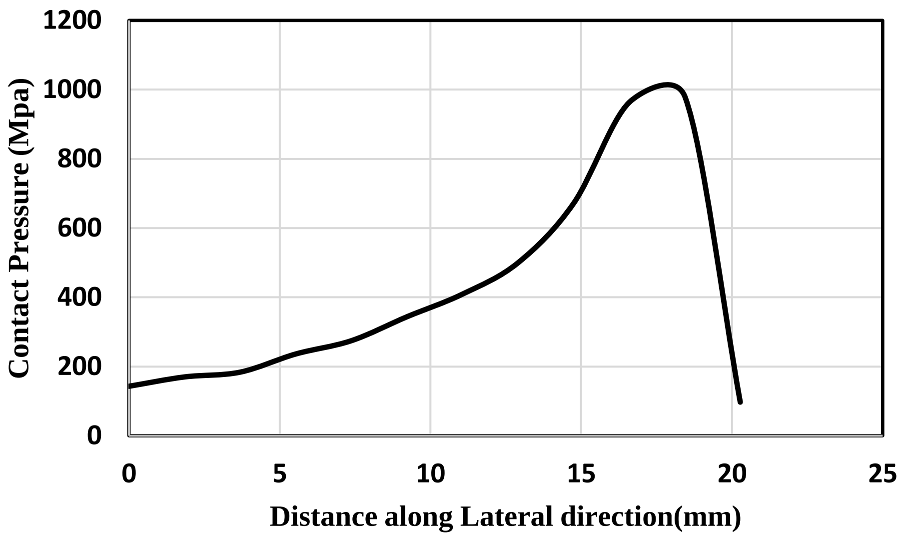

Figure 4-2 Contact pressure distribution on wheel surface along rolling direction

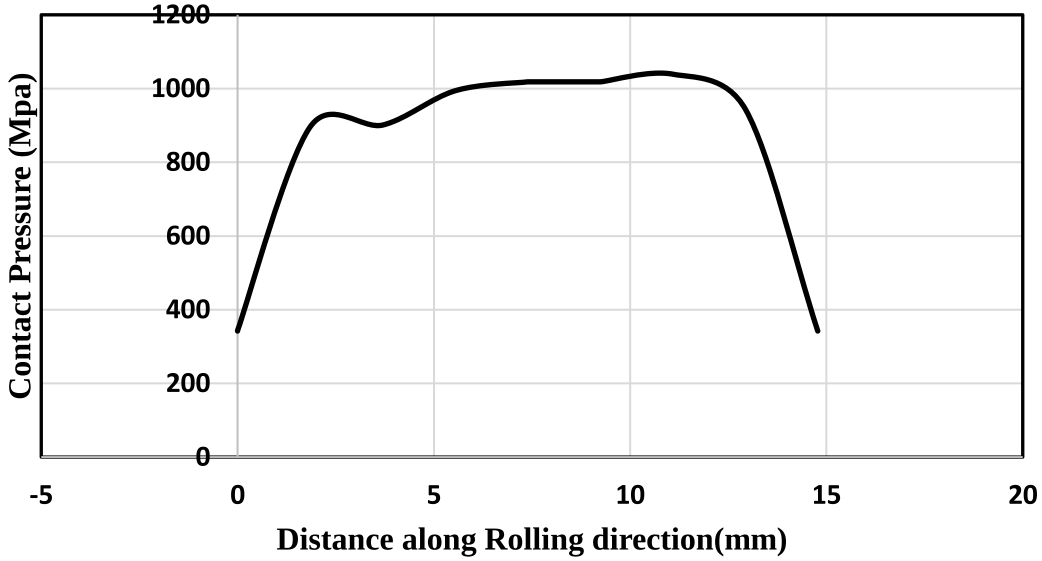

Figure 4-3 Contact pressure distribution on wheel surface along lateral direction

4.1.2 Surface and subsurface stresses

4.1.2.1 Von-mises stress:

Von-mises stress distribution at the wheel tread surface and different cross-sections is depicted as shown in Figure 4-4. The maximum von-mises stress was found on the surface of the wheel.

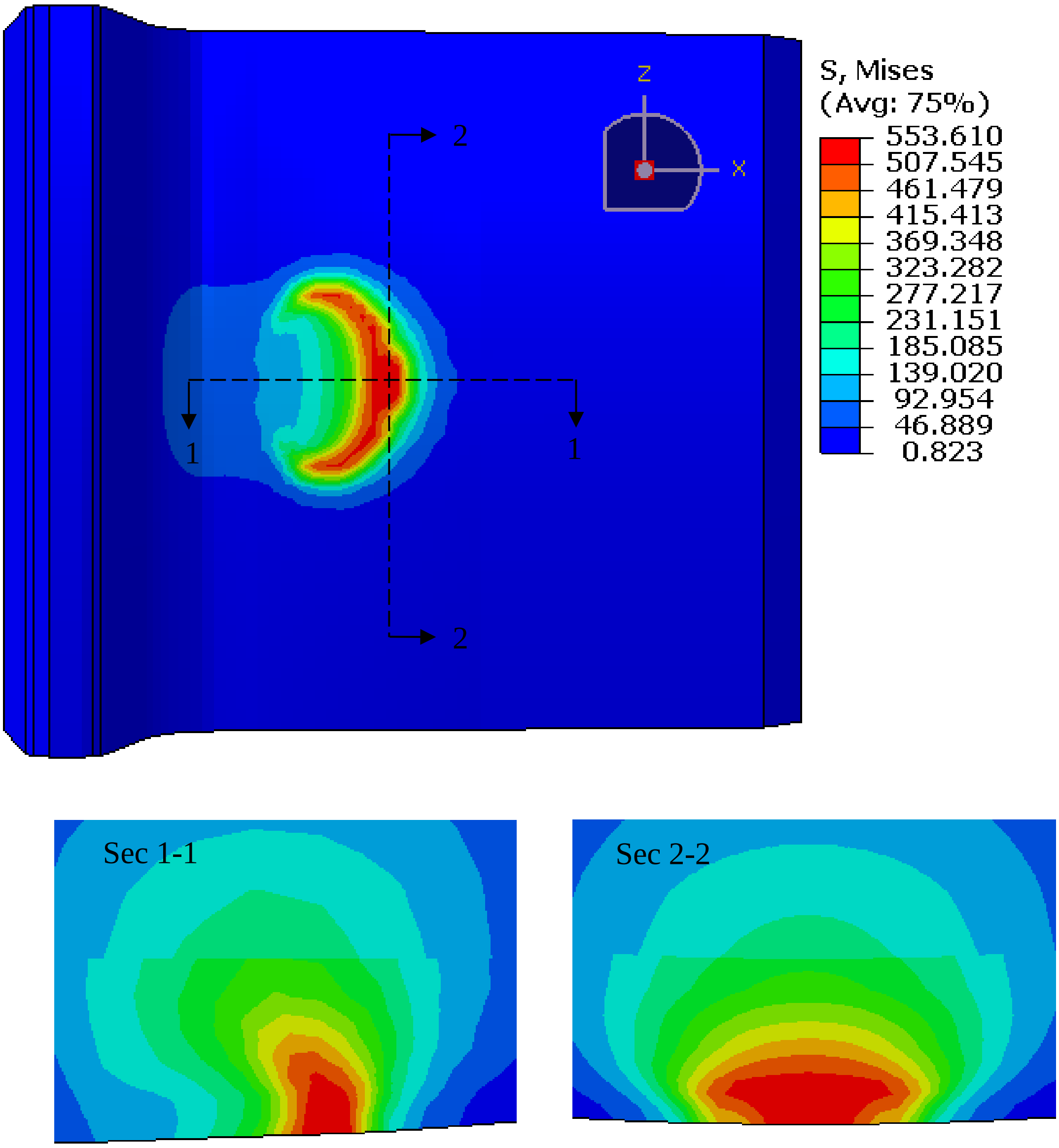

Figure 4-4 Von-Mises stress distribution of wheel from both left and front section

4.1.2.2 Shear stress:

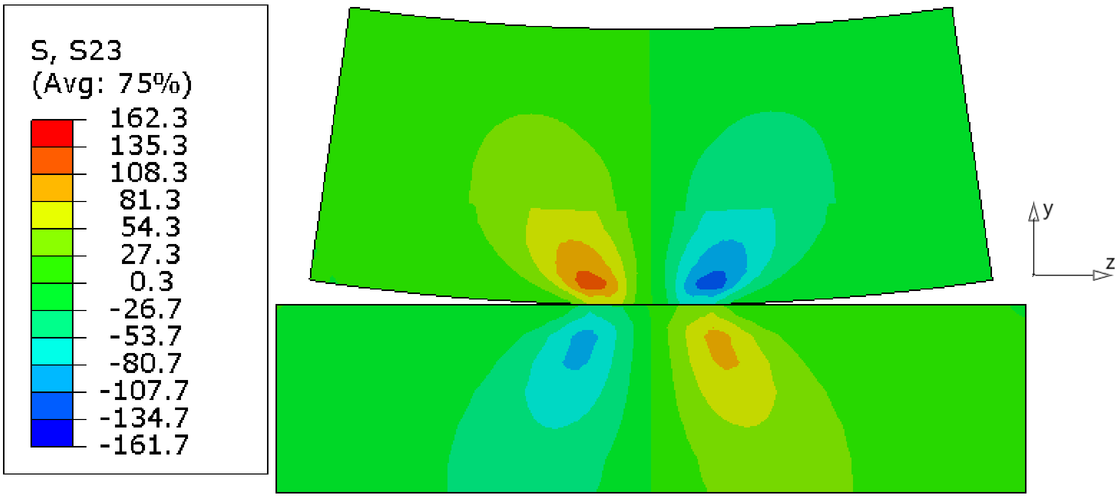

Figure 4-5 Distribution of τ_{yz} (S23)

4.1.2.3 Normal stress:

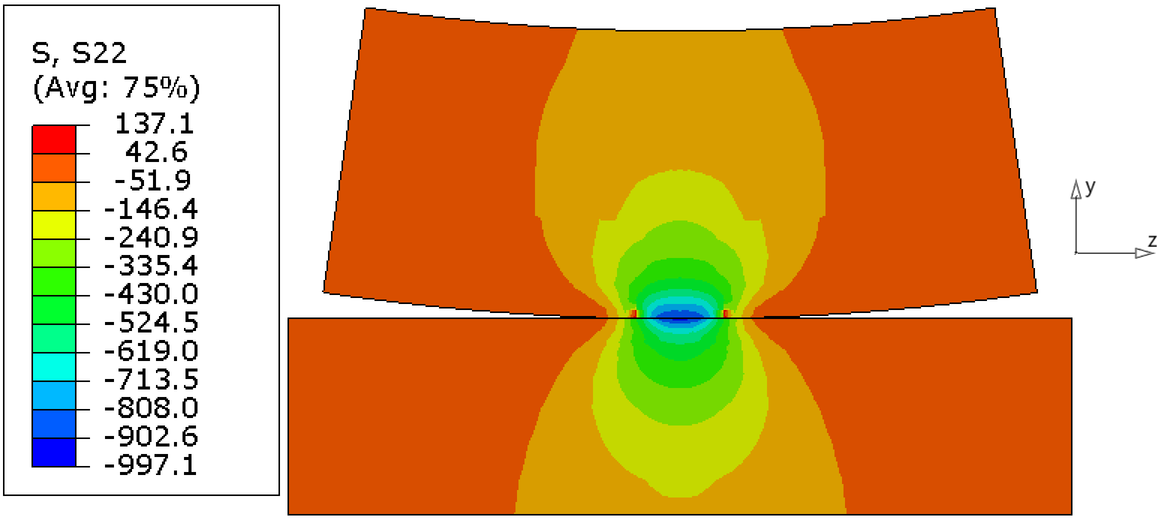

Figure 4-6 Distribution of σ_y(S22)

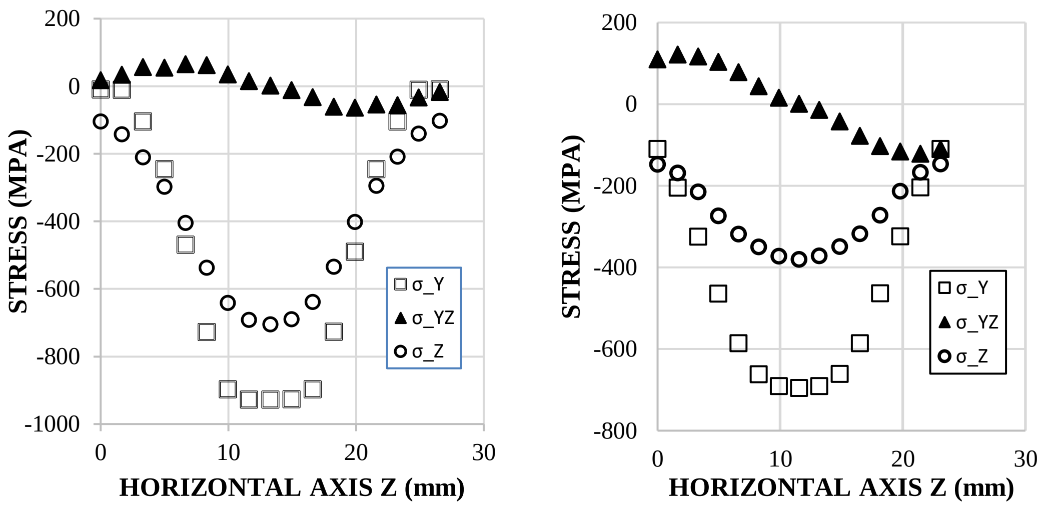

Figure 4-7 Stress plots of the wheel at x=0, y=0 (left) and x=0, y=2.6mm (right)

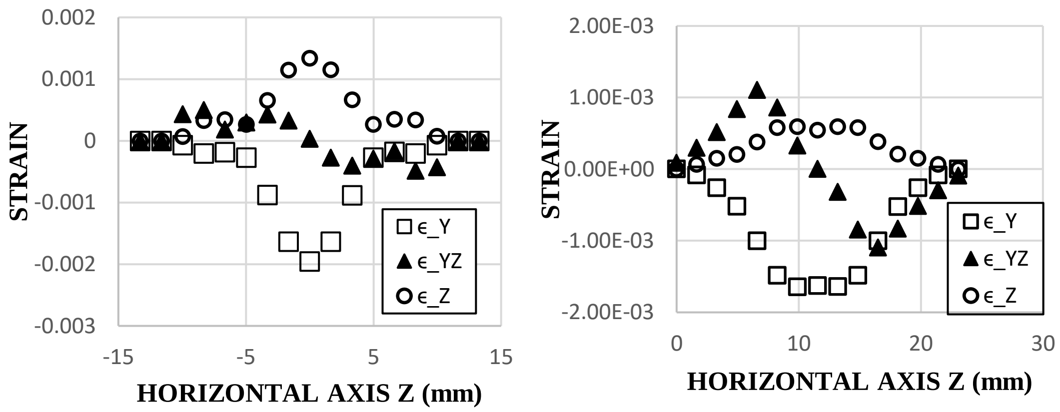

Figure 4-8 Strain plots of the wheel at x=0, y=0 (left) and x=0, y=2.6mm (right)

The stress and strain plots shown in Figure 4-7 and Figure 4-8 are approximated using a sinusoidal response as shown in Figure 3-22. Here it is important to note that the horizontal axis (z-axis) was replaced by the time using the equation below.

$$\boldsymbol{z/R = \omega t} \qquad \textbf{4-1}$$

Where, z is horizontal distance, ω is the angular velocity of the wheel, R is the wheel radius and t is the time.

4.1.3 Investigation of the Crack Orientation

In this section, study of the orientation of the crack including both depth and angle are conducted.

4.1.3.1 Crack Depth

Some studies like El-Sayed et al [15] paper apply the damage theory where depth of crack initiation is assumed to be at a point of maximum von-mises stress. However, the investigation at wheel load of 160kN and 0.3 friction coefficient shows depth of crack initiation (where the fatigue parameter is maximum) is at 2.6mm below the wheel surface even if the location of maximum von-mises stress is at the wheel surface. This due to the fact that failure of the wheel is highly dominated by the shear strain and shear stress and these shear components are higher below the surface as shown in Figure 4-5, Figure 4-7, Figure 4-8 and Figure 4-9.

The maximum fatigue parameter (FP) at various depths in the wheel are also investigated as shown in Figure 4-10. As illustrated in the figure, the fatigue parameter increased as the depth increased until the maximum fatigue parameter is achieved at 2.6 mm. Once the maximum FP is reached it will decrease as we further go deeper.

a)

b)

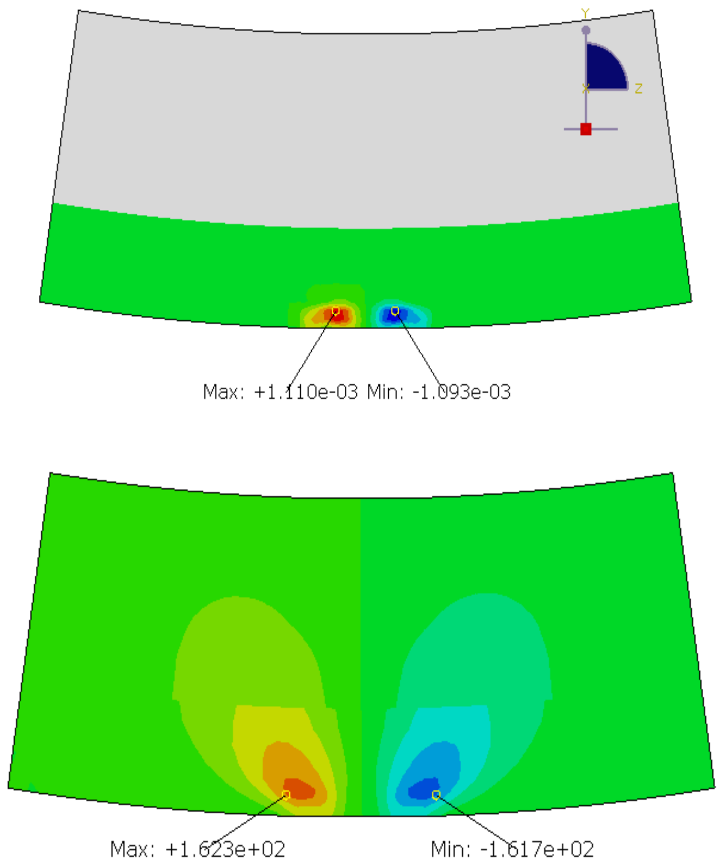

Figure 4-9 Distribution of (*a*) shear strain, γ_{yz} and (*b*) shear stress, τ_{yz}

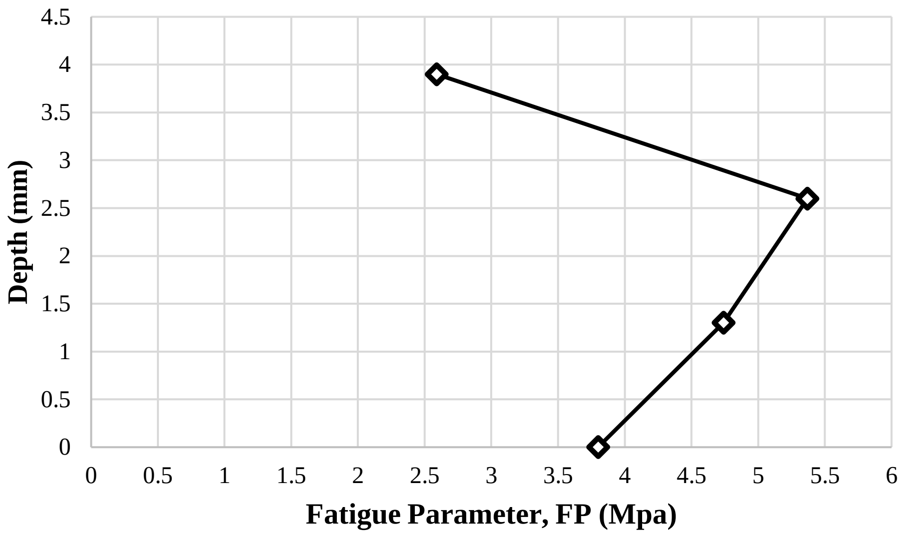

Figure 4-10 An illustration of change in fatigue parameter with wheel depth

Table 4-2 Investigation of fatigue damage along the wheel depth in the vicinity of contact

No	Node label	Location Depth, y(mm)	Maximum von-mises stress (MPa)	Maximum equivalent plastic strain, PEEQ (%)	Maximum fatigue parameter, FP_{max} (MPa)	Fatigue life Nf(cycles)
1	1144	0	567	0.804	3.80	66,326
2	9945	1.3	553	0.804	4.74	46,154
3	10010	2.6	549	0.520	5.40	37,327
4	9932	3.9	523	0.160	2.59	125,602
5	486	5.8	517	0.023	0.37	>1,000,000

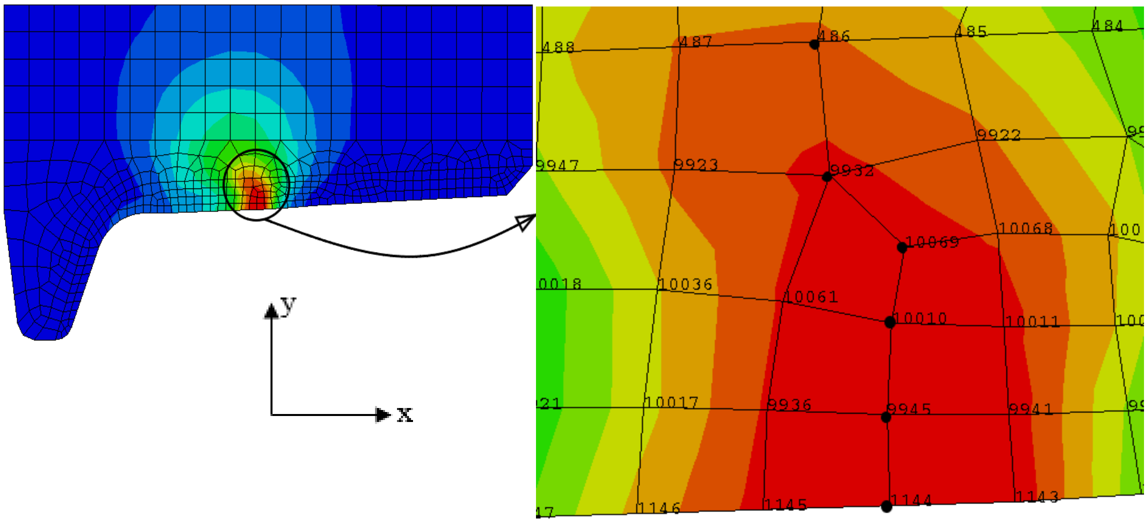

Figure 4-11 Node Labels along the depth

4.1.3.2 Crack Angle

To fully understand crack orientation the angle of crack initiation (nucleation), θ should also be known. This is the angle where the fatigue parameter becomes maximum. The MATLAB algorithm was used to search for the plane θ with maximum fatigue damage parameter (FPmax). The possible angle of crack initiation at four depth location was predicted searching for planes where the fatigue parameter, FP attains its maximum value.

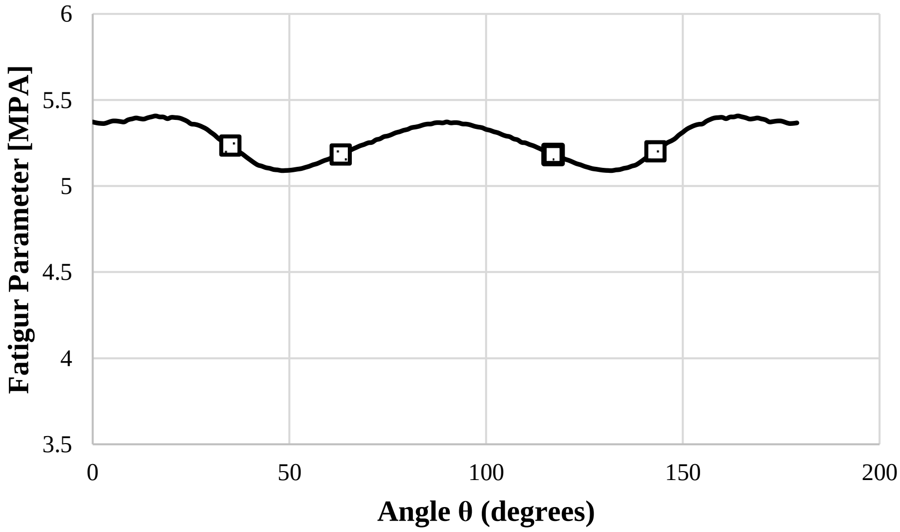

Figure 4-12 An illustration of the search of the critical plane 2.6mm below the surface

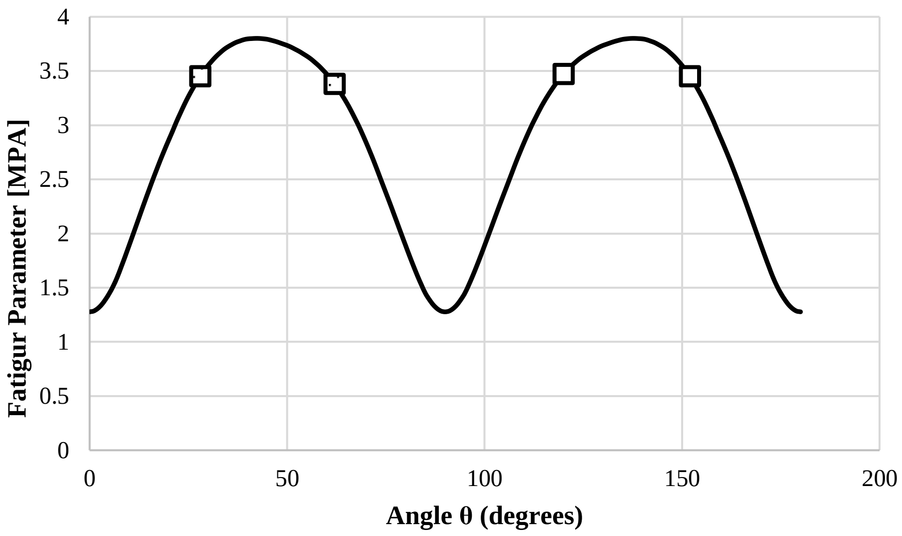

Figure 4-13 An illustration of the search of the critical plane at the surface (maximum von-mises stress)

It turned out that the predicted crack angle differs for the two cases considered in Figure 4-12 and Figure 4-13. Taking the range of 5 % from the maximum fatigue damage, the predicted crack angle range for the first case (at 2.6mm depth) is on (0^0, 40^0), (62^0, 123^0) whereas for the second case (at the surface) the predicted crack orientation was on the range (30^0, 58^0) and (120^0, 152^0).

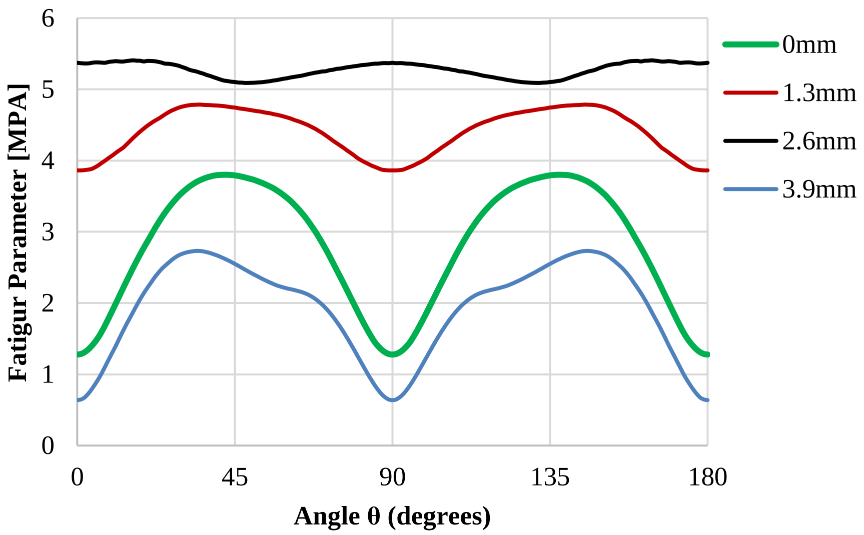

Figure 4-14 An illustration of the search of the critical plane at different depths

For the wheel depth 0mm, 1.3mm, and 3.9mm the fatigue parameter curves have almost similar trend and achieve maximum FP at closer range of angles, whereas the trend at depth of 2.6 mm is different from the others.

4.2 Parametric study

The influence of several factors on the fatigue life of the wheel are studied on this section using finite element and critical plane models proposed above. The effect of the following factors on fatigue life are considered; vertical loads, friction coefficient, wheel diameter.

4.2.1 Vertical loads

The effect of the vertical loads on fatigue life is studied at a straight track with wheel diameter of 660mm and friction coefficient of 0.3. The vertical loads in Table 4-3 were taken for investigation.

Table 4-3 Effect of Vertical load on fatigue life at friction coefficient of 0.3

Loading condition	F (KN)	FP_{MAX} (MPa)	N_f	Log(Nf)
L1	110	2.48	135,141	5.13
L2	140	4.10	58,529	4.76
L3	160	5.40	37,327	4.57
L4	180	6.84	25,466	4.40
L5	200	8.39	18,343	4.26
L6	220	10.15	13,531	4.13

As expected, the fatigue life decreases as the vertical load increases. As shown in Table 3-1 and Figure 4-15, the endurance limit is not achieved under the investigated loads.

4.2.2 Friction coefficient

Three conditions when μ = 0.2, 0.3, 0.4 are taken for investigation of friction effect at wheel load of 160kN and diameter 660mm as shown in Table 4-4 and Figure 4-15. The investigation shows that an increase in coefficient of friction has decreased the fatigue life of the wheel.

The application of boundary and elastohydrodynamic lubrication can lower coefficient of friction between wheel and rail (increasing fatigue life) at a risk of unexpected and invisible subsurface crack initiations.

Additionally, the analysis revealed that the depth of the most damaged element (with maximum fatigue parameter, FPmax) depends on the value of friction coefficients. Figure 4-17 shows for the friction consideration μ = 0.2 and μ = 0.3, the maximum fatigue parameter is found at depth of 2.6mm and 3.9mm below the wheel surface, respectively. For friction coefficient considerations μ = 0.4, maximum fatigue damage (location of crack initiation) is found on the surface of the wheel.

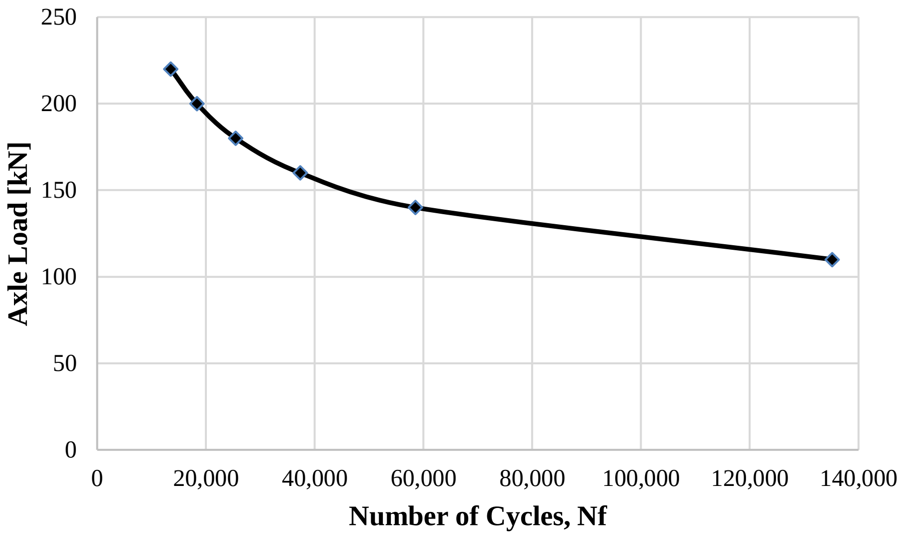

Figure 4-15 An illustration of variation of fatigue life with the vertical axle load

Table 4-4 Effect of Friction on fatigue life at F = 160kN

Friction coefficient, μ	Fatigue Parameter, FPmax	Fatigue life, Nf	Log(Nf)
0.2	4.0	60,954	4.78
0.3	5.4	37,327	4.57
0.4	9.6	14,642	4.16

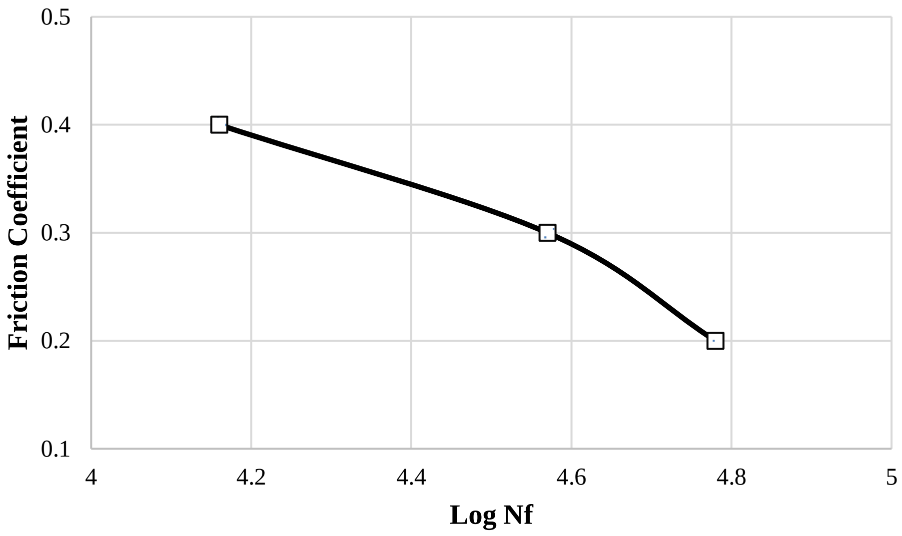

Figure 4-16 Variation of fatigue life with coefficient of friction

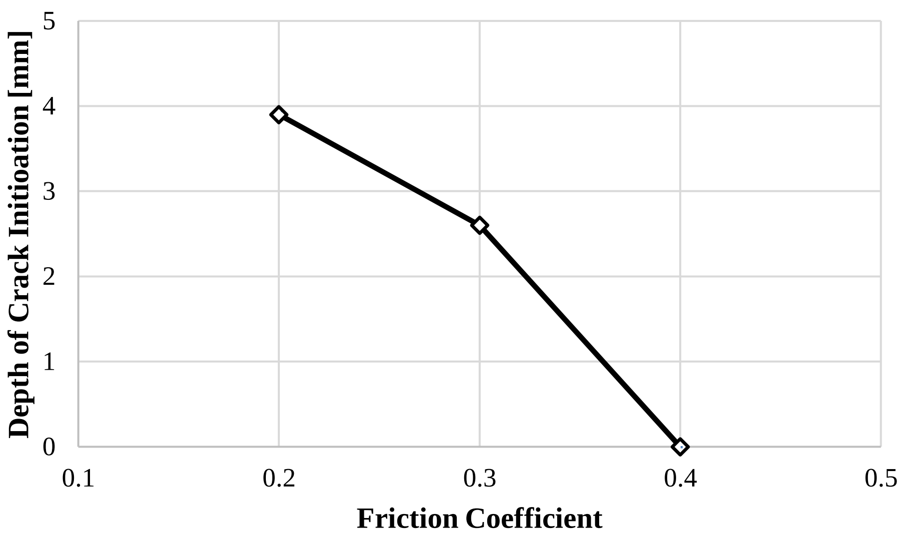

Figure 4-17 Location (Depth) of Crack Initiation at Varying Coefficients of Friction

4.2.3 Wheel diameter

The wheel diameter influences the fatigue damage, because according to the Hertz theory, the radius of the wheel will have effect on contact stress in the wheel. Different set of numerical simulations of wheels with different diameters, from 0.66 m to 1.02 m are used for investigation, as depicted in Figure 4-18. The result has shown that larger wheels can last longer than the smaller ones.

Table 4-5 Effect of wheel diameter on fatigue life

Wheel diameter (mm)	FP_{MAX} (MPa)	N_f (10^5)	Log(Nf)
660	5.4	0.373	4.57
800	4.3	0.541	4.73
1020	3.5	0.759	4.88

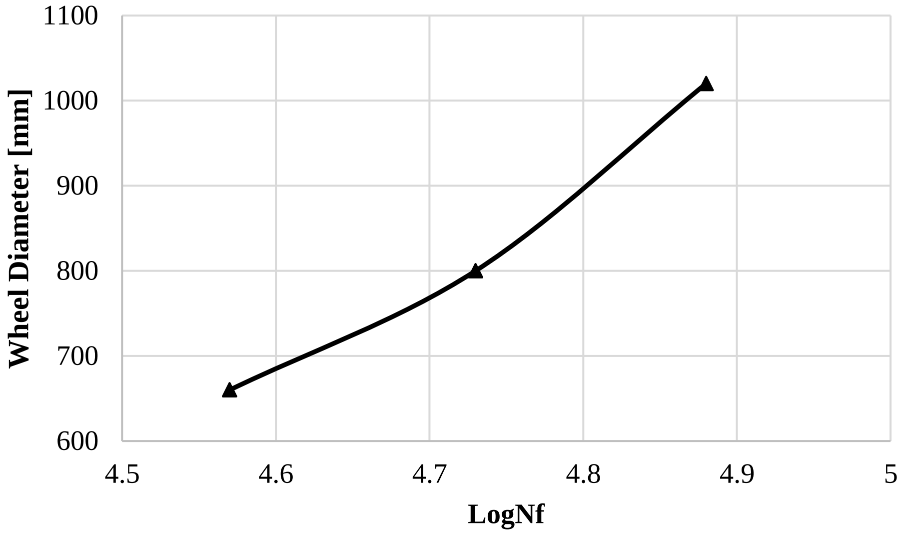

Figure 4-18 Variation of fatigue life with wheel diameter

4.3 Comparison with Experimental Work

In this section, a comparison between the results of an experimental work done by Jiang et al [26] and results obtained in this paper is made. In the experiment specimens made from steel S640N were investigated under various loading conditions. Among specimens tested those with closer loading path of wheel-rail loading were investigated.

The loading conditions used in those specimens were inserted to the numerical model and fatigue criteria developed to determine the fatigue lives. As shown in Table 4-6, about 36% of the specimens investigated under the prediction tool developed in this paper showed an error below 12% when compared to the experimental findings. The rest 64% of the specimens showed discrepancies with the predicted results.

The result suggests that the fatigue life estimation of the tool developed works best at low fatigue cycles and when the shear strain and shear stress are the major causes for crack initiation. For higher fatigue cycles and failures dominated by stress a numerical model with another set of material model and fatigue criteria should be adopted. Another possible reason for the discrepancy is that even though the specimens used in the test are loaded with similar loading paths, they do not consider the complex geometry in the wheel and rail model.

Table 4-6 Comparison of fatigue life experimental and numerical results

Specimen number	$\Delta\varepsilon/2$ (%)	$\Delta\gamma/2$ (%)	$\Delta\sigma/2$(MPa)	$\Delta\tau/2$(MPa)	N_f (exp.)	N_f (prediction)	Error (%)
126	0.3	0.52	436	277	1,050	1,188	11.8
138	0.3	0.52	440.2	273.4	767	823	7.3

$\Delta\varepsilon/2$ is axial strain amplitude, $\Delta\gamma/2$ is shear strain amplitude, $\Delta\sigma/2$ normal stress amplitude and $\Delta\tau/2$ is shear stress amplitude.